Deep models of integrated multiscale molecular data decipher the endothelial cell response to ionizing radiation

Ian Morilla, Philippe Chan, Fanny Caffin, Ljubica Svilar, Sonia Selbonne, Ségolène Ladaigue, Valerie Buard, Georges Tarlet, Béatrice Micheau, Agnes Francois, et al.

iScience

CellPress
OPEN ACCESS

Article

Deep models of integrated multiscale molecular data decipher the endothelial cell response to ionizing radiation

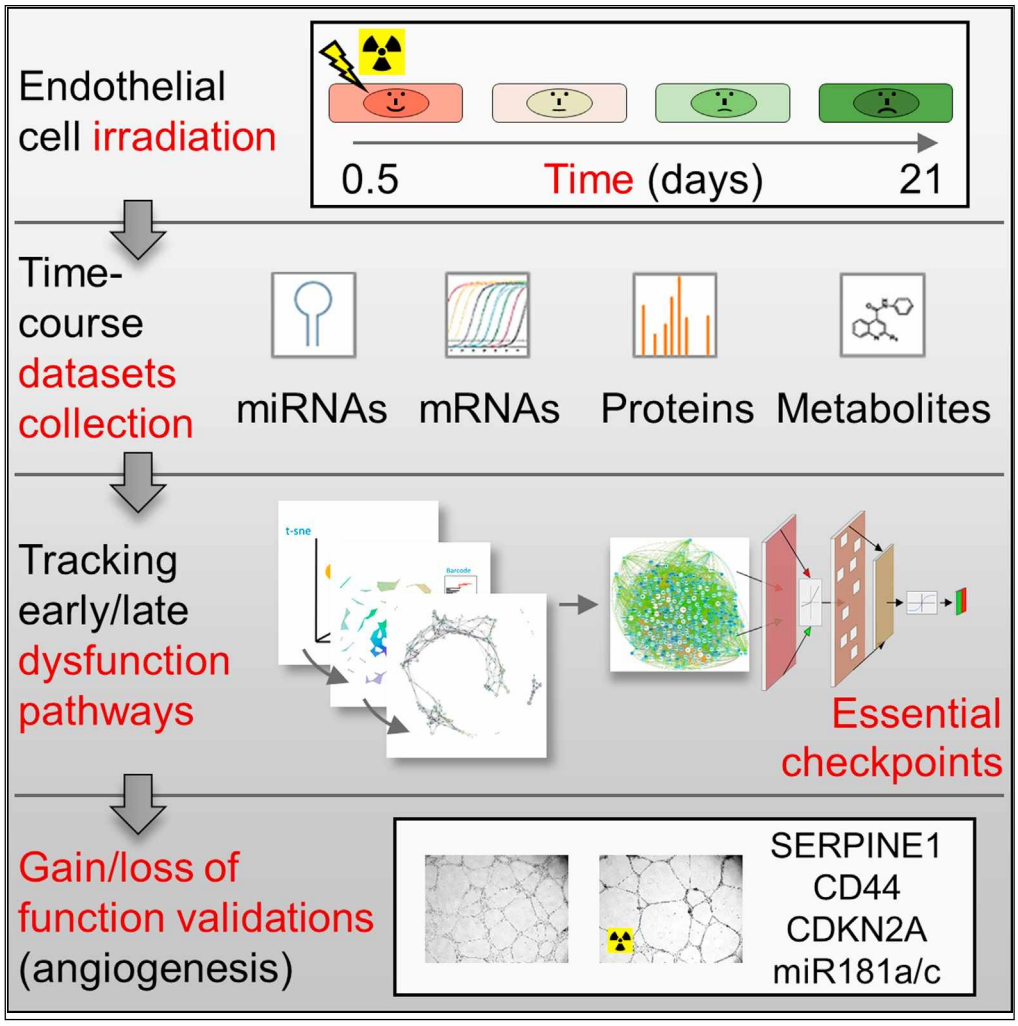

Ian Morilla, Philippe Chan, Fanny Caffin, ..., Mohamed-Amine Benadjaoud, Fabien Milliat, Olivier Guipaud

olivier.guipaud@irsn.fr (O.G.)
ian.morilla@gmail.com (I.M.)

Highlights

Irradiation promotes cell death, senescence, and impaired angiogenesis in HUVECs

Multi-omics analyses enable tracking pathways from early to late dysfunction

Dynamic modeling allows accurate learning of essential dysfunction checkpoints

Loss-/gain-of-function experiments identify key players of angiogenesis *in vitro*

Morilla et al., iScience *25*, 103685
January 21, 2022
https://doi.org/10.1016/j.isci.2021.103685

iScience

CellPress
OPEN ACCESS

Article

Deep models of integrated multiscale molecular data decipher the endothelial cell response to ionizing radiation

Ian Morilla,[1,*] Philippe Chan,[2] Fanny Caffin,[1] Ljubica Svilar,[3,4] Sonia Selbonne,[1] Ségolène Ladaigue,[1,5] Valérie Buard,[1] Georges Tarlet,[1] Béatrice Micheau,[1] Vincent Paget,[1] Agnès François,[1] Maâmar Souidi,[7] Jean-Charles Martin,[3,4] David Vaudry,[2] Mohamed-Amine Benadjaoud,[6] Fabien Milliat,[1,8] and Olivier Guipaud[1,8,9,*]

SUMMARY

The vascular endothelium is a hot spot in the response to radiation therapy for both tumors and normal tissues. To improve patient outcomes, interpretable systemic hypotheses are needed to help radiobiologists and radiation oncologists propose endothelial targets that could protect normal tissues from the adverse effects of radiation therapy and/or enhance its antitumor potential. To this end, we captured the kinetics of multi-omics layers—i.e. miRNome, targeted transcriptome, proteome, and metabolome—in irradiated primary human endothelial cells cultured *in vitro*. We then designed a strategy of deep learning as in convolutional graph networks that facilitates unsupervised high-level feature extraction of important omics data to learn how ionizing radiation-induced endothelial dysfunction may evolve over time. Last, we present experimental data showing that some of the features identified using our approach are involved in the alteration of angiogenesis by ionizing radiation.

INTRODUCTION

Radiation therapy, alone or in combination with other therapeutic strategies, is one of the most effective treatments for cancer. However, the radioresistance of tumors and the toxicity to healthy tissues present in the irradiation field are two major limitations regarding this treatment. Despite consistent improvements in ballistic configurations, there is still a point of no return at dose-volume thresholds that cannot be crossed without severely altering the patient's quality of life.

Profoundly modified by ionizing radiation, the vascular endothelium is in the spotlight to improve the overall benefit/risk ratio of radiation therapy (Guipaud et al., 2018; Wijerathne et al., 2021). New interdisciplinary approaches are useful to better understand radiation-induced biological effects and thus optimize radiation therapy outcomes for patients. These approaches can provide a comprehensive understanding of the response of the different cellular compartments involved in normal tissue and tumor responses and could therefore increase the likelihood of cancer cure and/or decrease toxicity to normal tissue. Molecular changes after exposure to ionizing radiation are numerous and of multiple types. They include molecular changes at the transcriptional, translational, and post-translational levels, phenotypic alterations, as well as deregulation of the microenvironment through the production and secretion of soluble factors such as reactive oxygen and nitrogen species, chemokines, cytokines, and growth factors. The cascade of molecular alterations triggered by irradiation may determine the phenotype of endothelial cells and alter the function of the vasculature, thereby contributing to the initiation and progression of radiation-induced damage in healthy organs and/or causing the recruitment of immune cells into tumors following radiation therapy (Guipaud et al., 2018; Korpela and Liu, 2014). In this regard, recent cancer therapies have successfully combined an effective immune response with radiation therapy (Zitvogel and Kroemer, 2015). On the other hand, strategies based on the endothelium for therapeutic gain in radiation oncology attempt to protect the vasculature of normal tissues from damage due to radiation, for instance by protecting endothelial cells from death, or by inhibiting vascular inflammation and endothelial cell activation. Because early alterations of endothelial cells by ionizing radiation are associated with late endothelial dysfunction (Rannou

[1]IRSN, Radiobiology of Medical Exposure Laboratory (LRMed), Human Health Radiation Protection Unit, 92260 Fontenay-Aux-Roses, France

[2]Normandie Univ, UNIROUEN, PISSARO Proteomic Platform, 76821 Mont Saint-Aignan, France

[3]Aix Marseille Univ, INSERM, INRA, C2VN, 13007 Marseille, France

[4]CriBioM, Criblage Biologique Marseille, Faculté de Médecine de la Timone, 13205 Marseille Cedex 01, France

[5]Sorbonne University, Doctoral College, 75005 Paris, France

[6]IRSN, Radiobiology and Regenerative Medicine Research Service (SERAMED), 92260 Fontenay-Aux-Roses, France

[7]IRSN, Radiobiology of Accidental Exposure Laboratory (LRAcc), Human Health Radiation Protection Unit, 92260 Fontenay-Aux-Roses, France

[8]These authors contributed equally

[9]Lead contact

*Correspondence: olivier.guipaud@irsn.fr (O.G.), ian.morilla@gmail.com (I.M.)

https://doi.org/10.1016/j.isci.2021.103685

et al., 2015; Toullec et al., 2018), it is critical to better understand the continuum and dynamics of molecular changes that propagate over time and lead to vascular injury.

In this work, we propose a systemic analysis of ionizing radiation-induced dysfunction in vascular endothelial cells using topological data analysis (Zomorodian and Carlsson, 2004) and deep learning on graphs (Hamilton et al., 2017a, b). Both of these approaches are enhanced by systems biology methods (Heinonen et al., 2015, 2018; Herskind et al., 2016) that significantly improve the characterization of biological processes across the heterogeneous samples of omics layers assembled for this study. These datasets describe the proteome, targeted transcriptome, metabolome, and miRNome of primary human endothelial cells grown *in vitro*, and the results are aligned with experimental validation steps. Briefly, this interdisciplinary approach was carried out in three main steps. First, we defined two feature representations of the data, i.e. early and late cell dysfunction based on the proximity of the sample to the response of vascular endothelial cells to irradiation over time at an irradiation dose of 20 Gy. This distinction allowed us to identify the molecular signatures of vascular dysfunction on each dataset. To do this, we used persistent homology algorithms based on discrete Morse theory (Scoville, 2019). We then integrated each signature into a global gene regulatory network (OGRN) (Chen and Mar, 2018), which led to identification of the global molecular signature. Last, this network was dynamically modeled using semi-supervised learning of the two feature representations (Ding et al., 2018), providing the top five candidates per feature for experimental validation. Ultimately, this methodology improves interpretable molecular hypotheses, providing radiobiologists with a systems biology approach useful for proposing potential endothelial targets to protect normal tissues from radiation and/or increase tumor control with radiation therapy.

RESULTS

In this work, we sought to exploit temporal molecular data from unirradiated and irradiated primary human endothelial cells (HUVECs) to identify key molecular players involved in the development of radiation-induced vascular dysfunction. To this end, we analyzed four levels of molecules, namely miRNAs, transcripts, proteins, and metabolites, to better understand the molecular response of HUVECs (Figure 1). The following results were derived from a systematic modeling approach encompassing multifaceted high-throughput screening, topological data analysis, homology, functional analysis, regulatory network reconstruction, and dynamic learning based on convolutional networks. We first present the recurrent temporal profiles of the data that were projected onto a 3D space where we found topologically important modules by homology. We then applied a network projection theorem capturing such homology in a practical way. Next, we analyzed the functional systems that the components of these modules deregulate. We subsequently considered the integration of molecular entities most likely to act as regulators in the molecular pathways of interest. This regulatory network helped us to understand the dynamics of the endothelial cell response to irradiation by constructing convolutional networks associated with each of the two characteristics considered, i.e. early and late responses. Last, we highlight an important biological process altered by radiation exposure, namely angiogenesis, and propose candidate genes to target in order to improve the effects of ionizing radiation.

Behavior of HUVECs postirradiation

After irradiation at 20 Gy, the cell layer became progressively less dense, likely due to death-induced cell detachment (Figure 2A). The dose of 20 Gy led to the loss of about 66% of the cells at day 4, 80% at day 7, 86% at day 14, and 93% at day 21, as compared with the nonirradiated cells (Figure 2C). At the same time, the cells became larger and displayed a higher amount of proteins and RNA per cell (Figures 2B and 2C), suggesting that they were still metabolically active. At 21 days after 20 Gy, on average 85% (40% at day 7) of the remaining cells were β-gal positive (Figure 2D), suggesting that almost all cells were senescent at this time point after irradiation.

Dataset time profiles

We collected 4 omics datasets from unexposed HUVECS and HUVECS exposed to 20 Gy of ionizing radiation (12 h–21 days after irradiation, 8 time points) (Figure 1). For the miRNomics and the transcriptomics studies, we focused on microRNAs (miRNAs) and genes of interest using TaqMan array microfluidic cards to assess levels of expression using RT-qPCR. We thus generated expression matrices containing the $2^{-\Delta Ct}$ values of 293 miRNAs (Data S1) and 308 gene transcripts (Data S2) over time. For the proteomics study,

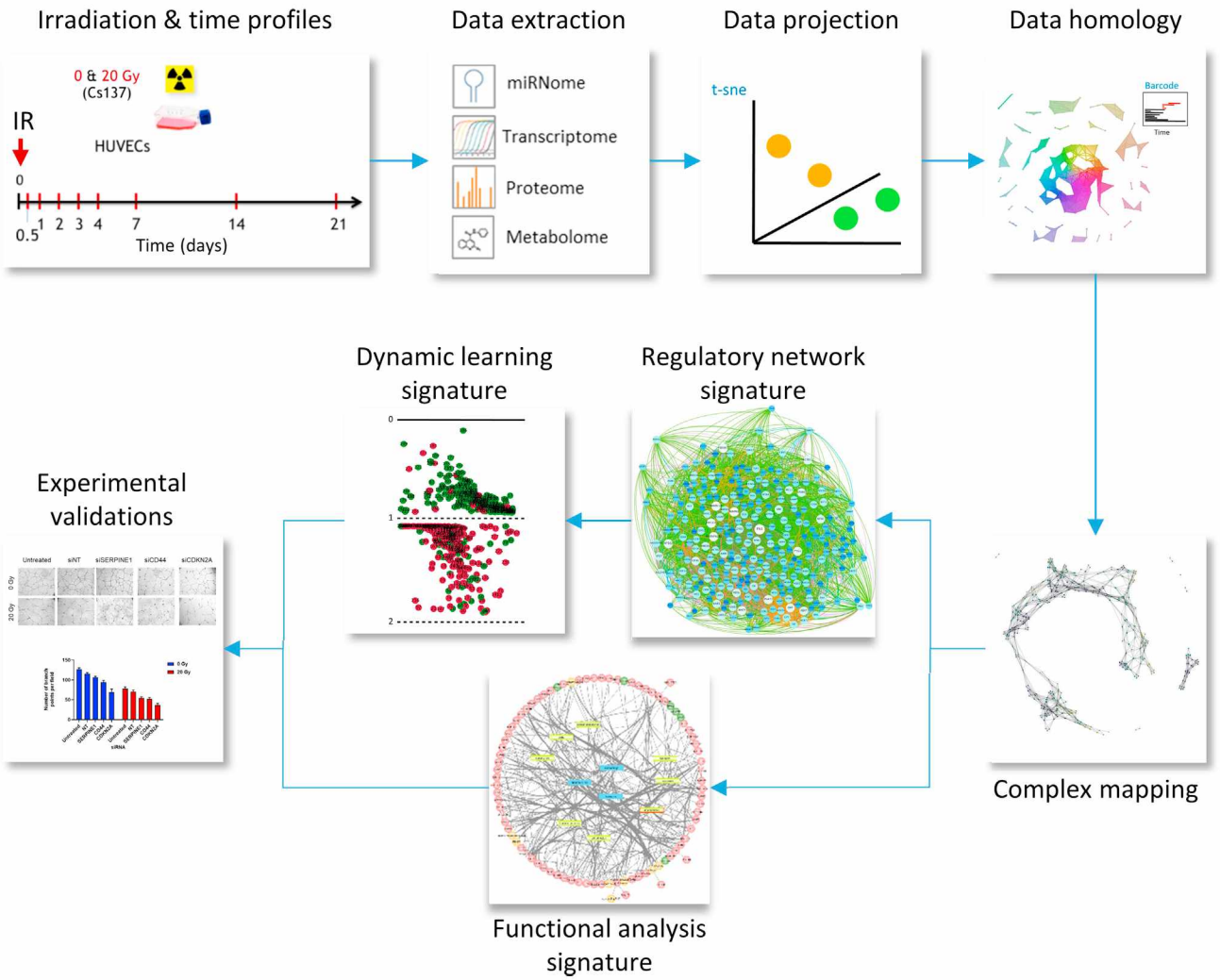

Figure 1. The main workflow leveraged in this manuscript

Time vectors were defined based on endothelial cell response measurements and omics data collection over time, i.e. miRNAs, targeted transcripts, proteins, and metabolites. Then, projection of omics layers in a lower space through t-SNE were used to seek recurrent homology between data by means of alpha complex building, enabling the construction of complex networks and determination of average data expression per homological module. Functional analysis of the identified signature and progression over time of the signature depending on the early or late response of the endothelial cells to irradiation were explored using deep learning modeling to propose targets of interest in connection with a cellular process altered by irradiation. Finally, candidates were studied experimentally using gain-of-function and loss-of-function strategies.

we performed quantitative iTRAQ LC-MS/MS analysis following isoelectric point-based peptide fractionation. This enabled the identification and quantification as a ratio of 4 exposed to 4 unexposed samples associated to a credible interval of about 1,700–2,800 proteins per time point (Data S3). For the metabolomics study, we achieved semi-quantitative ultra-high-performance LC-MS/MS. Using the LC-MS annotation with bank in-house tab enabled the quantification and identification of 115 metabolites for each technical replicate and each time point (Data S4).

From the 3D t-SNE projection of the clustered omics datasets (Figure S1A), we can visualize three differentiated time vectors depending on sample closeness to the response of HUVECs to irradiation. Thus, we defined T_1 as the acute vector composed by the measures captured in the range between days 0 and 7 postirradiation, T_2 as the mid-acute vector captured on day 14 postirradiation, and T_3 as the late response captured on day 21 postirradiation. Data were then translated into sets of NIR (nonirradiated) and IR (irradiated) elements describing the number of samples captured at each time depending on the irradiation dose and the time vector, i.e. T_k k = 1, 2, or 3, in which they were placed.

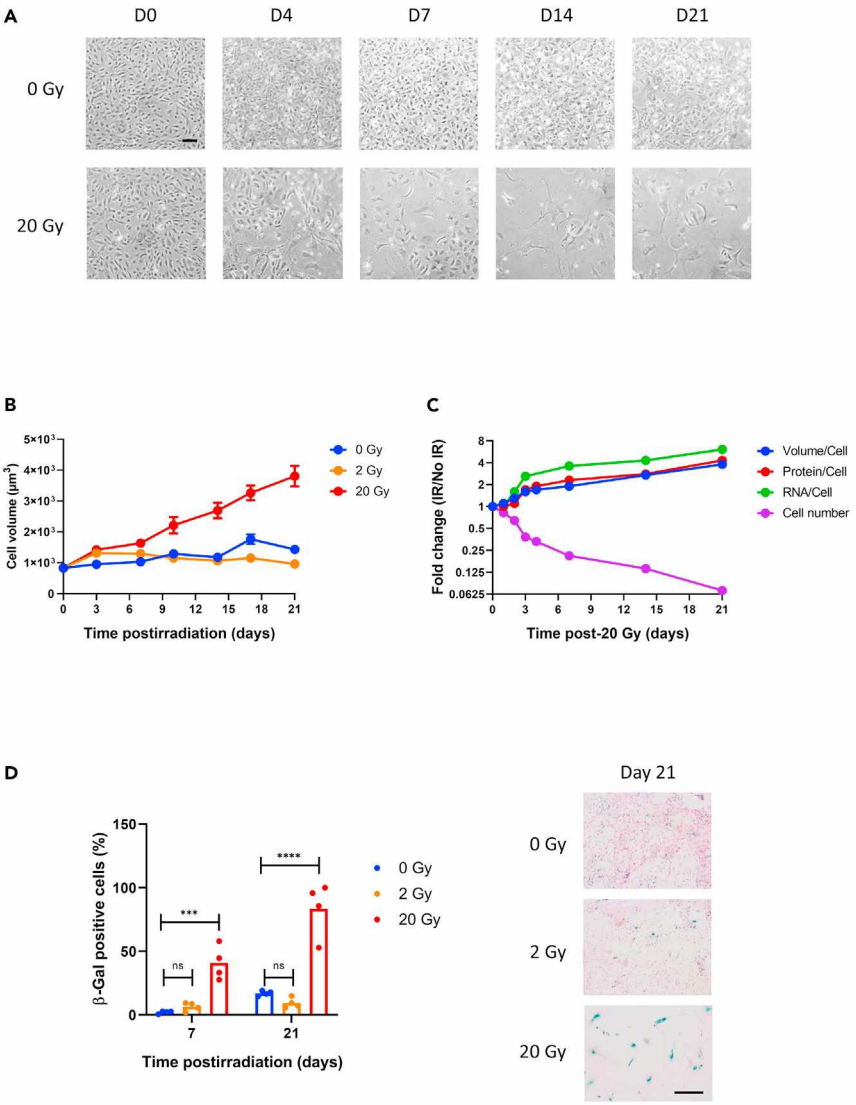

Figure 2. Endothelial cell behavior over time after irradiation: confluence, shape, number, volume, RNA and protein contents, and senescence

(A) Representative images of HUVECs on the day of irradiation and 4, 7, 14, and 21 days after irradiation at 20 Gy compared with nonirradiated cells. Scale bar, 50 µm.

(B) Estimation of the cell volumes of HUVECs after irradiation at 0, 2, and 20 Gy. n = 12 technical replicates.

(C) Estimation of changes in cell volume, number, and RNA and protein contents of HUVECs at different time points after irradiation at at 20 Gy compared with nonirradiated cells.

(D) Estimation of the proportion of senescent cells 7 and 21 days after irradiation at 0, 2, and 20 Gy. At the indicated time following 0, 2, or 20 Gy, cells were stained using a β-Gal Staining Kit. N = 4 technical replicates. One-way ANOVA test with Tukey correction. ns, not significant, ***$p \leq 0.001$, ****$p \leq 0.0001$. Representative images of HUVECs 21 days after irradiation are displayed on the right of the panel. Scale bar, 50 µm.

Tracking the pathway from early and nonirradiated to late endothelial dysfunction

Next, evaluating the barcodes associated with each omics dataset allowed us to accurately assign an optimal number of persistent modules (Figure S1B), herein referred to as *p-cubes*, to each mapper graph (see Videos S1, S2–S5). This assignment was also confirmed by checking the landscape and silhouette distributions of each omics barcode (Figures S1C and S2). We could then locally characterize each mapper graph as NIR or early cell dysfunction versus IR or late cell dysfunction regions. This distinction is based on the homology score average displayed by the molecular entities that compose the p-cubes.

In particular, the proteomics mapper graph (Video S3) is determined by 7 p-cubes. This relatively high number of cubes mainly traces the full path going from early to late endothelial cell dysfunction following a dose of 20 Gy. In contrast, the other omics datasets showed a much lower number of p-cubes: the transcriptome by 3 p-cubes (Video S4), the miRNome, and the metabolome by 2 p-cubes (respectively Videos S2 and S5). From Videos S2–S5, we observe how the mapper graph is described by p-cubes tracking the path going from NIR to early IR. This trajectory is homologically relevant in terms of the time vectors Ts for a dose of 20 Gy. The miRNA mapper graph is characterized by NIR to mid-IR full time path, also associated with a dose of 20 Gy. Next, the transcriptomics mapper graph, mainly associated to 20 Gy irradiation, aptly describes the transition from NIR to late-IR with a temporary delayed pass by early IR cell dysfunction.

Global molecular signature of the irradiated endothelium

Molecules in each omics dataset subject to functional reprogramming were identified by considering overlapping entities in the p-cubes assembly performed by the mapper algorithm. Subsequently, a thorough examination of the mapper graphs described in the previous section identified 83 candidate checkpoints controlling the response of endothelial cells to irradiation (Table 1). We inferred miRNA targets from the TarBase database, one of the embedded databases in DIANA webtools, leading to the identification of the CDKN2A gene as a target of *hsa*-miR-10b-5p, which is strongly linked to radiation-induced senescence *in vitro* and *in vivo* (Lafargue et al., 2017; Soysouvanh et al., 2020).

Highly altered biological functions

We used the subnetwork enrichment analysis module of Pathway Studio software to search for enriched regulated processes for each of the four sets of checkpoint candidates learnt from dynamic modeling. The proteome graph mapping is largely characterized by key players implied in the earlier processes of vascular endothelium injuries caused by ionizing radiation. Mainly, there is an overabundance of entities related to cell death, cytotoxicity, ROS generation, and oxidative stress as well as senescence. Other more unspecific biological processes to describe vascular endothelium injuries such as endothelial cell proliferation, cell regeneration, and cell infiltration were also reported. Similarly, as for the proteome, general terms indicating cytotoxicity (cell damage), senescence (aging), endothelial cell proliferation, and cell infiltration (cell adhesion) are also screened in the transcriptome graph mapping. Groups of transcripts enriched in cell processes such as angiogenesis, inflammatory, and immune responses are reported. However, other processes mainly involved in neovascularization and proinflammatory phenotype are also highlighted. Similarly, the miRNA graph mapping records and displays an enrichment in entities related to inflammatory response as well as cell growth, cell death, cell differentiation, and angiogenesis. It also shows an alternative endothelial/epithelial-to-mesenchymal transition as typically occurs in fibrosis (Morilla et al., 2017). Further, terms describing the early stages of endothelial injury, such as cell proliferation, death, or senescence, seem to be characterized by cell-cycle dysregulation (G0/G1 and G1/S) and double-strand DNA repair. Last, the graph mapping associated with the metabolome contains metabolites enriched in the set of biological processes describing endothelial damage after irradiation. Supporting this, we found cellular processes associated with early stages of dysfunction, such as regulators of ROS generation, inflammatory response, and oxidative stress.

From the list of 83 candidate checkpoint entities obtained by dynamic modeling, we searched for clusters of molecular entities enriched in gene ontology (GO) annotations that ideally would be involved in common biological processes relevant to the radiation-induced response of endothelial cells. We have pinpointed the top 25 enriched GO cell process categories identified in this study by excluding overly general biological cell processes (Figure S3). An expected enrichment of some GO terms is related to death and programmed cell death (apoptosis), in agreement with previous studies, as well as terms related to a response to stress and to defense and inflammatory responses, in line with knowledge on endothelial cell response to DNA damage (Corre et al., 2010; Guipaud et al., 2018; Korpela and Liu, 2014). Interestingly, more than half of the top enriched cellular processes may be directly or indirectly related to angiogenesis, suggesting that a large portion of the identified entities are related to angiogenesis and that this process is strongly altered by ionizing radiation in our study.

Taking this further, we used the subnetwork enrichment analysis module in Pathway Studio software to search for protein regulators and protein targets, and then we searched for enriched regulated processes and cells using the 83 candidates and 200 most enriched regulated proteins (Figure 3). The network built using Pathway Studio and Cytoscape (Figure 3B) confirms the previous analysis of GO pathways/groups enriched with the 83

Table 1. Proposed checkpoints controlling the response of endothelial cells to irradiation in each omic layer

miRNA	Description/ alias	Transcript	Description/alias	Protein	Description/alias	Metabolite[b]	Description/alias
hsa-miR-10b[a]	hsa-miR-10b-5p	ADAMTS1	ADAM metallopeptidase with thrombospondin type 1 motif 1	AHCY	Adenosylhomocysteinase	Alanine	
hsa-let-7b-5p				ALDOA	Aldolase, fructose-bisphosphate A	Aminoadipic acid	
hsa-let-7d-5p				CDCA3	Cell-division-cycle-associated protein 3	AMP	
hsa-miR-15b-5p		BHLHA15	Basic helix-loop-helix family member a15 (also named BHLHB8)	DDX6	DEAD-box helicase 6	Aspartate	
				EIF4E	Eukaryotic translation initiation factor 4E	D-arabinonic acid	D-arabino-1,4-lactone
hsa-miR-16-5p				ESD	Esterase D		
hsa-miR181a							
hsa-miR181c		CD44	CD44 molecule (Indian blood group)	FGFR1	Fibroblast growth factor receptor 1	Fumarate	
hsa-miR-191-5p				FN1	Fibronectin 1	Galactitol	
hsa-miR-19a-3p		EPHB4	EPH receptor B4	GANAB	Glucosidase II alpha subunit	Guanosine	
hsa-miR-210-3p		FABP5	Fatty acid binding protein 5	GPX1	Glutathione peroxidase 1	Leucine	L-leucine
hsa-miR-218-5p				GRB2	Growth factor receptor bound protein 2	Maleic acid	
hsa-miR26a-1[1]	hsa-miR-26a-1-3p	IL18	Interleukin 18	HBA1	Hemoglobin subunit alpha 1	Methionine	
		LRRC2	Leucine rich repeat containing 2	HMGB1	High-mobility group box 1	N-acetylserine	
hsa-miR-26b[1]	hsa-miR-26b-3p			LRPPRC	Leucine-rich pentatricopeptide repeat-containing protein	NMDA	N-methylaspartate
hsa-miR-320a-3p						Pantothenic acid	
hsa-miR-365a-5p		MAPK14	Mitogen-activated protein kinase 14	MCTS1	MCTS1 re-initiation and release factor	PPi	
hsa-miR-374a-5p							
hsa-miR-532-3p		MCL1	MCL1 apoptosis regulator, BCL2 family member	MMRN1	Multimerin 1	Tryptophan	L-tryptophan
hsa-miR-5582-3p				NUTF2	Nuclear transport factor 2		
hsa-miR-92a-3p				PABPC4	Poly(A)-binding protein cytoplasmic 4		
		NFKBIA	NFKB inhibitor alpha	PLOD1	Procollagen-lysine,2-oxoglutarate 5-dioxygenase 1		
		PDE4B	Phosphodiesterase 4B				
		SELP	Selectin P	PSMB3	Proteasome 20S subunit beta 3		
		SMAD3	SMAD family member 3	RPL13	Ribosomal protein L13		
		TIMP3	TIMP metallopeptidase inhibitor 3	RPL24	Ribosomal protein L24		
				RPL26	Ribosomal protein L26		
		TNFSF10	TNF superfamily member 10	RTN4	Reticulon 4		
				SERPINE1	Serpin family E member 1		
				SPARC	Secreted protein acidic and cysteine rich		
				TAGLN2	Transgelin 2		
				TMEM263	Transmembrane protein 263		
				TPM1	Tropomyosin 1		
				TPM2	Tropomyosin 2		
				TUBB6	Tubulin beta 6 class V		
				VDAC1	Voltage dependent anion channel 1		
				VIM	Vimentin		

[a]Complementary arm of the "reference" miRNA; those are originated from the same hairpin structure (pri- and pre-miRNA). When the data are not sufficient to determine which sequence is the predominant one, the majority sense in DIANA database is considered and put inside brackets (see Supplemental Information text for further details on their gene targets).
[b]See Supplemental Information text for further details on their associated enzymes.

checkpoint candidate entities (cell death and apoptosis). In addition, it highlights other previously known processes involved in the response of endothelial cells to irradiation, i.e. aging and senescence, as well as a connection to the immune response through cell adhesion and relationships with leukocytes, especially macrophages. Last, it indicates angiogenesis as an important process in response to irradiation. Figure 4 shows an alternative representation of the network, keeping only angiogenesis as a cellular process. It indicates the level of expression of the candidates, showing different responses at early and late times.

Dynamic modeling enables accurate learning of essential checkpoints of vascular endothelial cell dysfunction after irradiation

We built a hybrid dynamic model based on the semi-supervised learning of vascular endothelial cell dysfunction after irradiation (Figure 5). Visualization of the model's performance (Figure S4) was achieved by applying a spectral graph convolution to the integrated omics graph as shown in an mp4 file (Video S6). The weighted average of the first model is 0.56 supported by 111 and 176 samples to the early and late feature representations, respectively. This figure increases to 0.79 in the second learning model. These measures asymptotically reach a steady state of accuracy close to 0.77 with the progressive inclusion of many tested layers up to 1,024.

Dynamic modeling thus enabled shortening of the initial molecular signature by the best candidates learned to be closest to the feature representations, i.e. both *hsa*-miR-10b-5p and *hsa*-miR-5582-3p at a similar level, MCL1, *hsa*-miR-181c-5p, RTN4, and SELP regarding the early cellular dysfunction on the one hand, and fumarate, adenosine monophosphate, *hsa*-miR-181a, and CD44 for the late dysfunction on the other hand. In addition, the model identifies the existence of an intermediate pattern composed of molecules such as TAGLN2 or SERPINE1 that trace the path from early to late dysfunction but end up halfway. It is conceivable that their reprogramming could prevent the effect of radiation-induced late dysfunction. In Figure 6, we display the interaction network of top candidates, cell processes, and radiation as a treatment, established on a bibliographic basis using the text mining module of pathway studio. This figure sums up the many relations between top candidates and between top candidates and cell processes such as cell damage, cell death, apoptosis, senescence, cell adhesion, immune response, and angiogenesis.

Angiogenesis as an essential cell process impaired by radiation exposure: experimental validation of some checkpoint candidates learned from dynamic modeling

We then focused on several targets highlighted by dynamic modeling to study their involvement in the alteration of tube formation after irradiation. We selected mir181c and CDKN2A (a target of miR10b) as features involved in the early dysfunction, SERPINE1 that traces the path from early to late dysfunction, and miR181a and CD44 for the late dysfunction. SERPINE1, CD44, and CDKN2A (at late time) were upregulated in radiation-exposed cells (Figures S5A and S5B). Surprisingly, miR181a and miR181c were hardly modulated after irradiation regarding the RT-qPCR results (Figure S5A), whereas dynamic modeling highlighted these 2 miRNAs as important features. This may possibly be caused by the closeness of these two miRNAs in expression to the homology generators observed during the complex creation. To obtain more information on their potential relevance in the response to irradiation, we measured their level of expression by RT-qPCR in the gut of mice exposed to ionizing radiation (Figure S6). The results show a statistically significant decrease in the expression of miRNA181a and miR181c on day 3 and day 7 after irradiation, confirming *in vivo* the result of the modeling. We also show that angiogenic genes ANGPTL1, interleukin-6 (IL-6), MMP2, and SERPINE1 were upregulated in the intestine exposed to irradiation (Figure S6B), suggesting a role of angiogenesis in response to tissue damage.

To establish the contribution of SERPINE1, CD44, CDKN2A, miR181a, and miR181c in angiogenesis *in vitro*, we used siRNAs and miRNA mimics in HUVECs and estimated tube formation on Matrigel after irradiation. The administration of siRNA against SERPINE1, CD44, or CDKN2A in unexposed or irradiated HUVECs showed 74%–88% inhibition of gene expression (Figure S7A). Regarding miRNAs, we verified that mimics enter durably into the cells (Figure S7B). Administration of miR181c mimic was deleterious for HUVECs at day 7 posttransfection (Figure S7C). Nevertheless, miRNA mimics led to an overexpression of both miR181a and miR181c at day 3 and day 7 posttransfection and following 20 Gy at day 5 postirradiation for the miR181a mimic (Figure S7D).

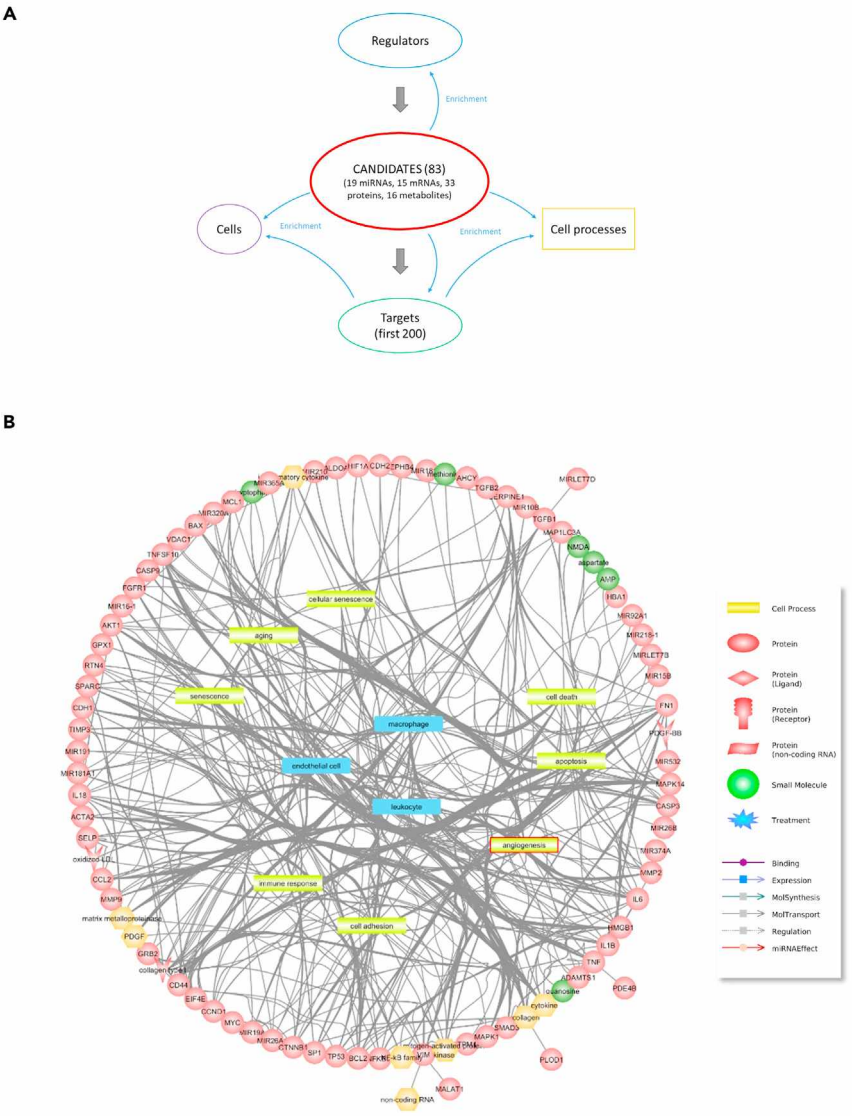

Figure 3. Common regulators and expanded cells, targets, and cell processes of selected candidates

Enrichment analyses using Pathway Studio software enable highlighting of essential processes potentially altered by exposure of endothelial cells to ionizing radiation.

(A) Strategy of enrichment: enrichment of common regulators and targets using the 83 candidates on the one hand, enrichment of cells and cell processes using candidates and targets on the other hand.

(B) Schematic view using Cytoscape of connections between candidates, common regulators, targets, cells, and cell processes. Angiogenesis appears as one of the cell processes potentially impaired by ionizing radiation.

We first checked that angiogenesis capacities of HUVECs were impaired by ionizing radiation exposure. Looking at untreated and nontargeting control siRNA conditions, a 40%–50% decrease in the number of branching points of HUVEC tubes formed on Matrigel was observed 18 h after irradiation at 20 Gy compared with unexposed cells (Figure 7). The administration of siRNAs against SERPINE1, CD44, and CDKN2A was associated with a marked impairment of the number of branch points in the tubes formed by HUVECs (Figures 7A and 7B). Also, siRNAs against SERPINE1 and CD44 induced a decrease in gene expression of CD34 (Figure S8A), a key player in angiogenesis (Siemerink et al., 2012). The administration of miR181a and miR181c mimics was associated with an increased number of branch points in tube formed by HUVECs after irradiation compared with untreated cells (Figures 7C and 7D) and influenced the expression of the essential angiogenic genes CD44, PDGFRA, and TIMP3 in nonirradiated cells and IL-6 and VEGFA in both nonirradiated and irradiated cells (Figures S8B and S8C). These results suggest that the

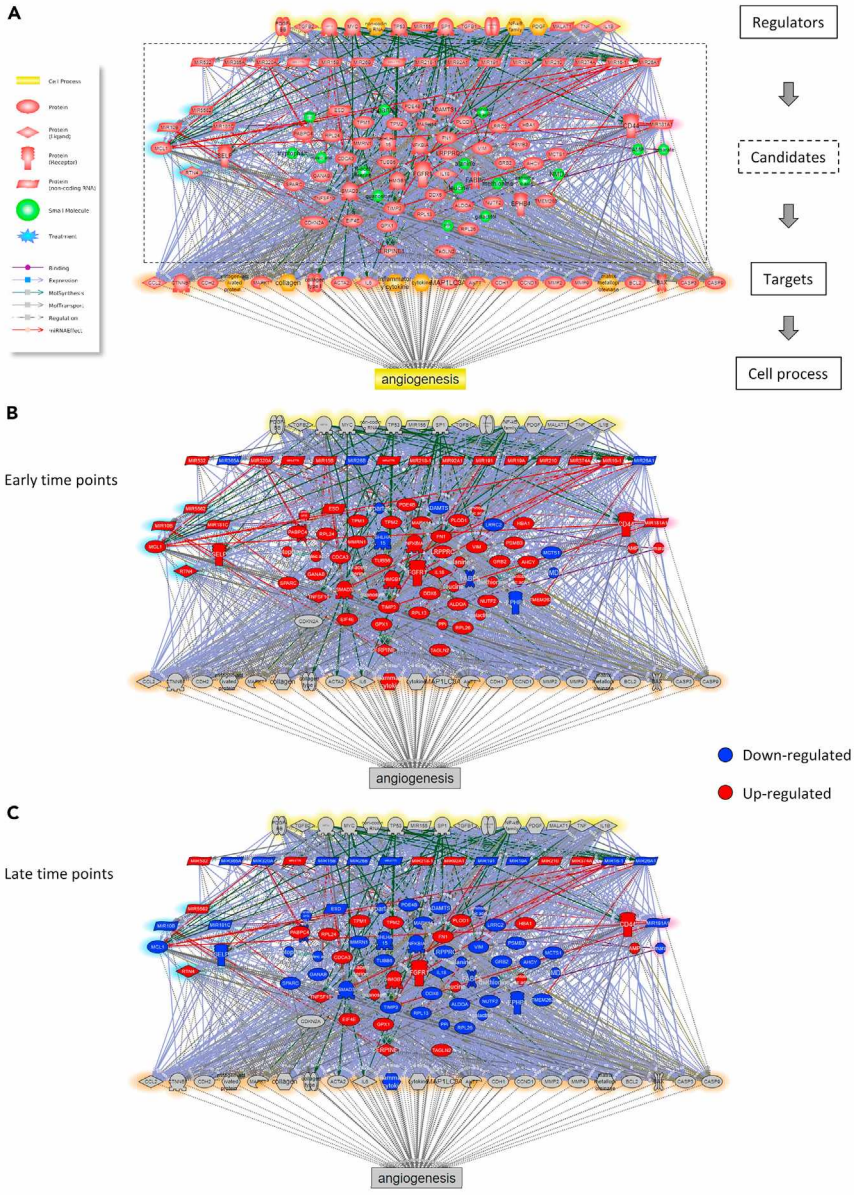

Figure 4. Interaction network of the 83 experimental candidate entities with their predicted regulators, targets, and the cell process angiogenesis

(A) Network overview obtained using Pathway Studio software. The 83 candidate checkpoints controlling the response of endothelial cells to irradiation in each omics layer are shown in the middle of the array, whereas the regulators and targets predicted by enrichment are placed above and below the candidates, respectively. Note that CDKN2A, an interesting miRNA target highlighted in our study, is also included in the network although not experimentally identified.

(B and C) Same network where candidate entities are pinpointed according to their level of expression compared with nonirradiated cells (red: increased expression, blue: decreased expression) in the early (0.5–7 days) (B) and late (14–21 days) (C) time points following irradiation.

radiation-induced alteration of angiogenic capacity may be partly counterbalanced by overexpression of miR181a and to a lesser extent miR181c.

DISCUSSION

The vascular endothelium represents a promising target for improving the therapeutic potential of radiation therapy in the future (Guipaud et al., 2018; Wijerathne et al., 2021). In this study, we used high single

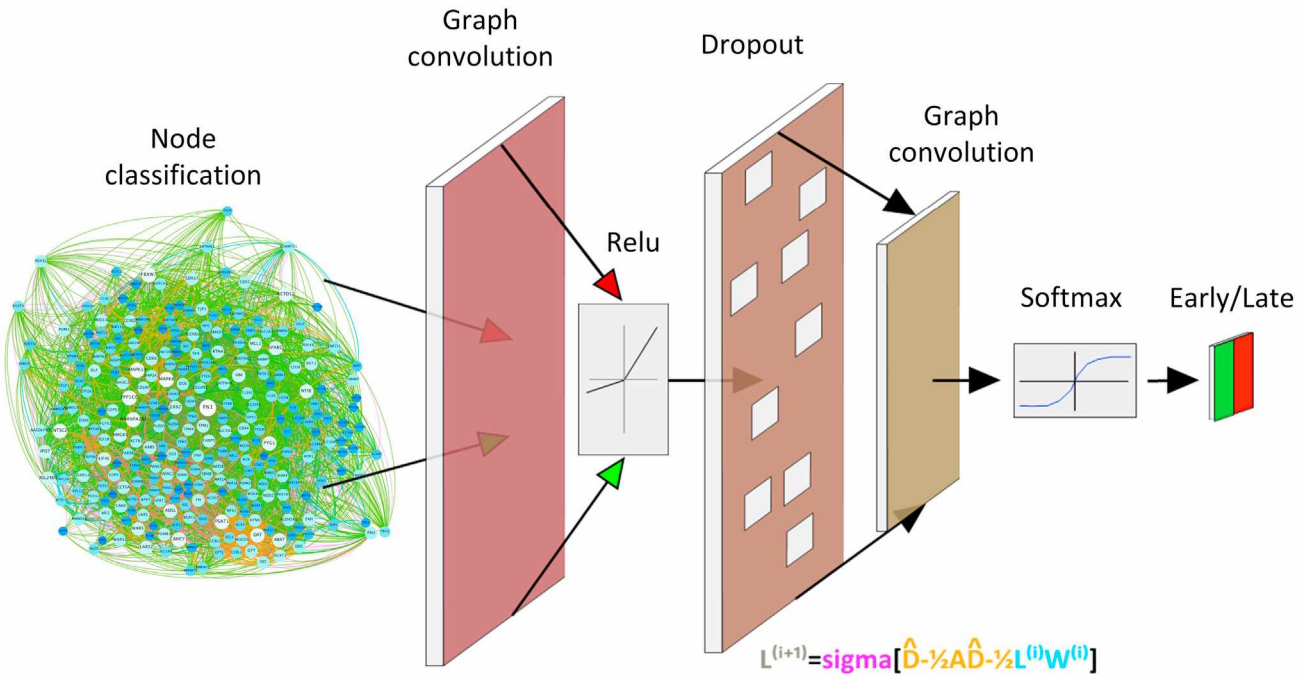

Figure 5. Classification of candidates in early and late dysfunction after ionizing irradiation

The figure presents an overview of the graphical learning model calibrated in this work to predict early or late-stage molecular dysfunction after ionizing irradiation. We operated in layer starting from the regulatory gene network with all potential associations between the selected candidates at the multiscale level. Each interaction of a pair was integrated into a first convolutional layer according to its early or late initial stage (highlighted in green and red, respectively). At the entrance of the first layer, all this information was merged (in red and green) with the other interactions of the network, which is why we have colored in dark brown as a reference in this layer. Then, we sorted all these associations by means of a ReLU activation layer. Because this is a sort of diffusion process from the original interactions to the output of the model, we have drawn lighter shades respecting the colors of the original arrows. Then, a 50% exclusion layer followed to avoid overfitting. There, the interactions associated with the first convolutional layer were probabilistically clustered (the colors become even lighter) while waiting for the applications of the last layers. A final convolutional layer was then designed to contain all the information about the aggregations associated with an initial pair of genes. Finally, we used Softmax activation to transform the probability distributions of the last convolutional layer into a binary matrix of information that will be the output of the model. This computation ensured the final prediction of the initial genes in an early or late dysfunctional stage. The equation: this equation describes how the machine learning model recursively passed through the layers, namely: (1) we normalized the network structure (highlighted in orange); (2) after normalization, we multiplied its structure by that captured by a previous epoch (i- > i+1). We called this the gene properties (highlighted in blue). Finally, we applied sigma to the gene properties and model weights (colored in pink). Sigma is a nonlinear function based on the Adam optimizer that computes the minimization problem associated with the loss of information produced between the eventual output of the model in a particular epoch and its immediately preceding solution.

doses of ionizing radiation, namely 20 Gy for HUVECs and 19 Gy for mouse intestine, which may seem far from conventional fractionated radiation therapy protocols that deliver daily dose fractions of 1.8–2 Gy.

The animal model we used was first established in rats to investigate the effects of localized irradiation in the long term (Hauer-Jensen et al., 1983) and then developed in mice (Zheng et al., 2000). The same team also developed a model in which a loop of small intestine was transposed into the left part of the scrotum in order to irradiate the intestine repeatedly (Hauer-Jensen et al., 1988, 1990). This model results in reproducible complications very similar to those observed in patients with acute or late radiation enteropathy and is considered a clinically relevant model (Hauer-Jensen et al., 2014). In addition, localized single-dose and fractionated irradiation to the small intestine caused in this model similar responses in the rats in terms of survival and radiation-induced pathology (Langberg et al., 1992). However, due to the small size of mice, this model can only be performed in rats. For all these reasons, it is considered that in mice, like in rats, a single dose of 19 Gy to a small part of the intestine induces late lesions such as those seen in patients treated with radiation therapy. Importantly, it is the only model that can generate radiation-induced intestinal fibrosis in mice. To better understand the adverse effects of radiation therapy, we therefore used this model of localized single-dose irradiation of the intestine as a model of radiation-induced late intestinal injury. We previously showed using this model of single-dose irradiation that endothelial cells played a critical role in the initiation and development of radiation-induced intestinal toxicity in mice (Rannou et al., 2015; Toullec

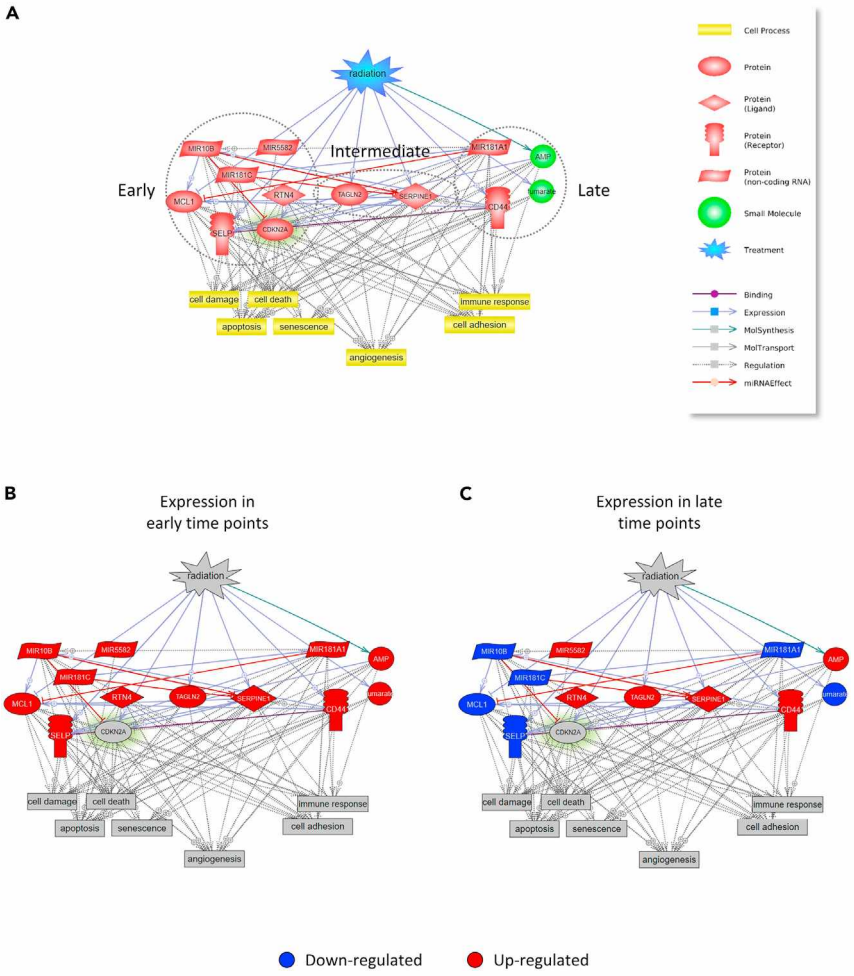

Figure 6. Interaction network of top candidates, cell processes, and radiation

(A) Protein network of the top candidates identified in this study, enriched cell processes, and the term "Radiation" as treatment was obtained using Pathway Studio software. The top 13 candidates include the top 6 entities for early dysfunction (*has*-miR-10b-5has*hsa*-miR-5582-3p, has1, *hsa*-miR-181c-5p, RTN4, and SELP), the top 4 entities for late dysfunction (fumarate, adenosine monophosphate, *hsa*-miR-181a, and CD44), and the top 2 entities for intermediate patterns (TAGLN2 and SERPINE1). CDKN2A, target of miR10B, is also included in the list of top candidates.

(B and C) Same network where candidate entities are identified according to their level of expression compared with nonirradiated cells (red: increased expression, blue: decreased expression) in the early (0.5–7 days) (B) and late (14–21 days) (C) time points following irradiation.

et al., 2018). On the other hand, advances in treatment planning and delivery now allow delivery of one or more high-dose ionizing radiation fractions (40–60 Gy in 1–5 fractions) to tumors by stereotactic body radiation therapy (SBRT) (Lo et al., 2010; Qiu et al., 2020), which is increasingly used to treat patients (Brown et al., 2019; Simone et al., 2013). Thus, we assume that endothelial cells from normal tissues and tumors can be exposed to one or more high-dose radiation fractions such as that used in our *in vitro* model and in SBRT.

The endothelial cell model of radiation-induced dysfunction we used has been extensively characterized in our previous work (Ben Kacem et al., 2020; Heinonen et al., 2015, 2018; Jaillet et al., 2017; Paget et al., 2019). In this model, at a dose of 20 Gy, the cells stopped proliferating as early as one day after irradiation and did not proliferate at all by the third day (Ben Kacem et al., 2020; Paget et al., 2019). In addition, we estimated that at day 7 post-20 Gy only 2%–3% of cells had divided, and at most once, during the first 7 days after irradiation (Paget et al., 2019). Here, we show that a dose of 20 Gy led to the progressive loss of almost all cells (7% of irradiated cells remained 21 days after exposure), probably due to cell death, and impaired the angiogenesis function of HUVECs. Also, our results suggest that these cells were metabolically active,

as they were larger and contain more RNA and proteins, and were probably all in senescence, as suggested by the result of β-gal staining. These results can be connected to cellular processes revealed by pathway enrichment analyses such as cell death, senescence, and angiogenesis, showing that our multi-omics approach can reveal processes observed experimentally at the cell culture level, which validates our method. Although this model is far from what endothelial cells undergo *in vivo*, several works suggest that irradiation leads to endothelial cell senescence, which would participate in radiation-induced late effects (Azimzadeh et al., 2015; Soysouvanh et al., 2020). In this sense, it could be hypothesized that endothelial cells remaining in irradiated tissues are senescent, dysfunctional, and contribute significantly to late radiation-induced damage. Considering all these data and our own results, this *in vitro* model could recapitulate the steps that lead irradiated endothelial cells to become senescent *in vivo*.

To decipher the molecular response of endothelial cells, we analyzed the miRNA, transcript, protein, and metabolite contents of primary vascular endothelial cells to model the continuum of radiation-induced injury processes between early and late vascular dysfunction in healthy tissue and tumors during radiation therapy. The great depth of omics datasets exploited is a major advantage of this analysis to fill the gap in our understanding between early and late endothelial dysfunction, which is thought to contribute significantly to the tissue effects of radiation therapy. This allowed us to propose molecular targets related to the radiation-induced alteration of angiogenesis, a fundamental function of endothelial cells.

Integration of multi-omics data identifies a molecular signature of radiation-induced endothelial dysfunction

Deep models of integrated multi-omics data enable learning the entire molecular process accurately (Eraslan et al., 2019). To build these models, we exhaustively interrogated a heterogeneous set of available kinetic samples using data shaping methods whose core comes from topological data analysis. The models successfully captured the complex molecular regulation between early endothelial cell response and late endothelial cell dysfunction, which likely occurs in radiation therapy and causes adverse effects despite dose fractionation (Christersdottir et al., 2019; Halle et al., 2010a, 2010b; Rannou et al., 2015; Toullec et al., 2018). After a thorough examination of the samples, we found that their temporal expression profiles showed three initial shapes that corresponded to the boundary points of the different experimental conditions associated with each measurement. In this way, this accumulation of samples suggests a real effect due to the time period considered after irradiation. Our analysis accounts for such an effect by translating each dataset into time expression matrices subject to these models. A regression of the datasets to their fold-change shapes allowed for proper interpretation of the results in the subsequent parts of the study. At some stages, a projection of the datasets preserving their original shape was useful to create the topological skeleton of each omics layer. In each of these discrete spaces, we were able to compare groups of elements in a homological way, converting these spaces into continuous omics spaces, conveniently represented by graphs (discrete Morse theory used in the mapper algorithm). This allowed us to identify topologically important molecular feature modules to perform continuous conversions between omics spaces, which goes beyond descriptive clustering. As the omics datasets are expressed in terms of the expression-time vectors introduced earlier, the molecules comprising these modules appear to be excellent candidates for forming the basis of the molecular signature describing the mechanisms from early to late endothelial cell dysfunction after irradiation.

From the molecular signature to a gene regulatory network

Because molecules do not function independently in the cell, we provide a global view of the exchanges produced in the response after ionizing radiation with the unsupervised integration of each molecular candidate as a gene regulatory network. In this respect, there is a high degree of homological similarity between the integrated omics graph and the graph resulting from the mapper algorithm of the identified persistent candidates. The former then relies on the topological representation of the data, which formalizes the notions of proximity, continuity, and robust denoising through an analytical study of spaces and maps. This perspective enables learning of global representations from local information, unlike more traditional methods that tend to rely on overly simplistic and less flexible assumptions (Munch, 2017). In particular, the global structure of our complex data can be rigorously quantified through those topological invariants. As invariant, those representations became ideal features to be used as the basis of the graph neural network (Tauzin et al., 2020), herein applied to dynamically learn molecular interactions and patterns (Knyazev et al., 2018; Rhee et al., 2018) occurring within cells after irradiation.

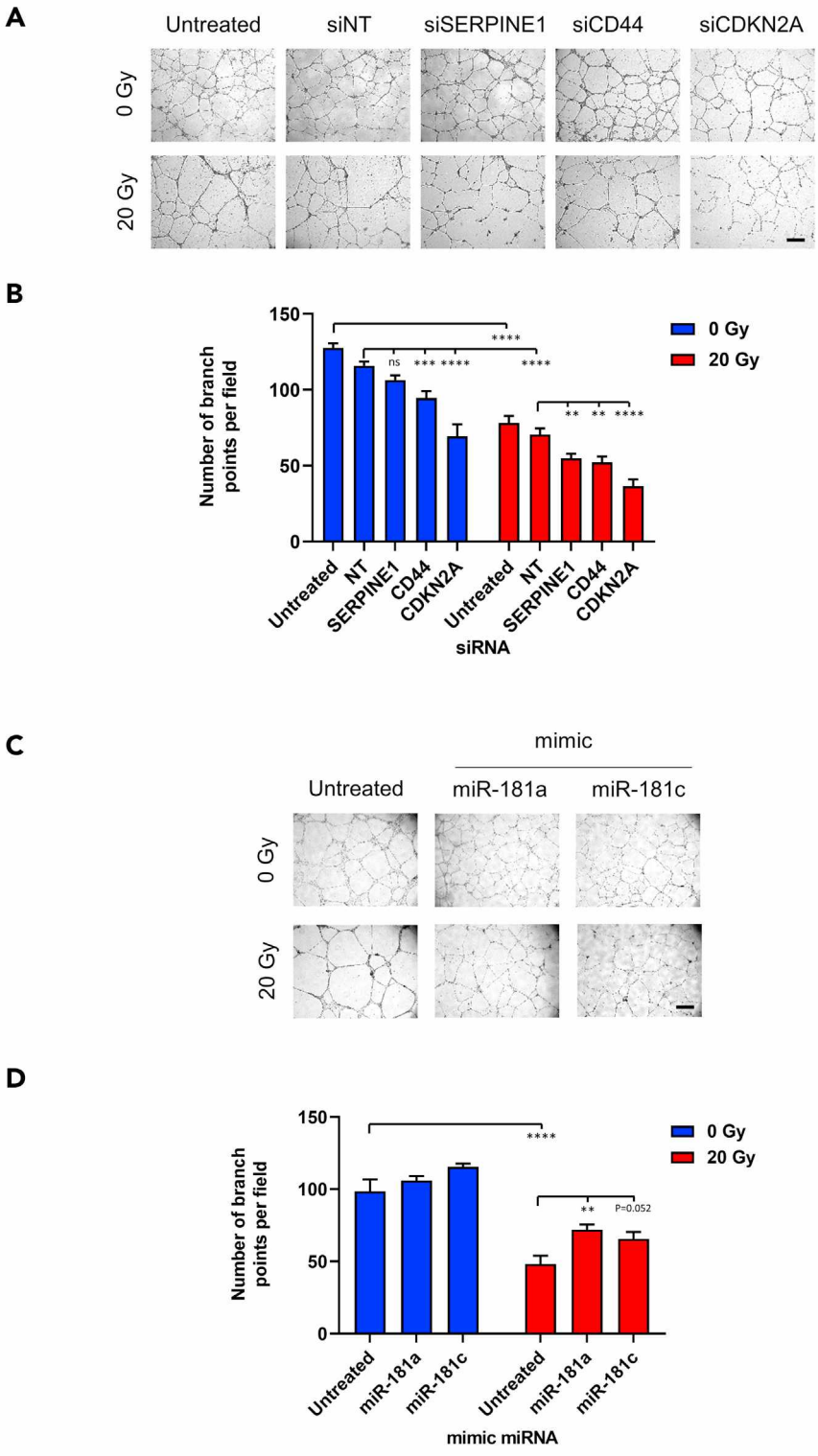

Figure 7. Tube formation in irradiated HUVECs treated with siRNAs or miRNA mimics

(A and C) Representative images of HUVECs seeded on Matrigel 18 h postirradiation at 20 Gy after treatment by siRNA against SERPINE1, CD44, or CDKN2A (A) or by miR181a or miR181c mimics (C). Scale bars, 400 μm.

(B and D) Number of branch points per microscope field of view were quantified and plotted. Data are mean ± SEM of three independent experiments. One-way ANOVA test with Sidak correction. ns, not significant, $^{**}p \leq 0.01$, $^{***}p \leq 0.001$, $^{****}p \leq 0.0001$.

Systems biology and pathway analysis identify the most promising molecules

The use of systems biology methods has greatly improved the extraction of relevant biological information about the full range of processes underlying endothelial dysfunction. From the graph mapping, we deduced three behavioral patterns with respect to molecular functions that could lead to toxicity during radiation therapy. These graphs are closely related to the earlier and intermediate mechanisms of response to endothelium injuries triggered by DNA/cell damage, apoptosis, senescence, cell migration, and angiogenesis. They primarily account for immune and inflammatory responses characterized by cell adhesion, and, ultimately, fibrosis predicted by the miRNome. These three sets of graphs accurately mapped the deregulated pathways required to release cellular stress along the endothelial barrier disruption as well as the alteration of the angiogenesis process. Their dynamics were obtained naturally by applying spectral convolutional aggregation on the nodes of the omics integrated network. Although there was no particular reason for these aggregations to be robust, we eventually found that they were. Thus, this process made possible to any given early, intermediate, and late feature representations of cells dysfunction, the semi-supervised learning of the aggregation process leading to a list of the most promising molecules to be experimentally validated: MCL1, SELP, RTN4, and CDKN2A as a target of the selected miR10b, SERPINE1, CD44, TAGLN2, miR10b, mi181a, miR181c, miR5582, AMP, and fumarate.

Biological relevance of the most promising molecules

Some of the 13 selected entities using the supervised learning have clearly direct links with irradiation. Upregulated by IL-6, the BCL2 homolog MCL1 has an antiapoptotic effect in HUVECs following radiation exposure (Chou et al., 2009). The vascular P-selectin (SELP) is a cell adhesion molecule that is upregulated in response to ionizing radiation and participates in the recruitment of leukocytes (Molla et al., 1999). The cyclin-dependent kinase inhibitor 2A (CDKN2A), also known as $p16^{INK4A}$, acts as a negative regulator of normal cell proliferation and is a marker for and an effector of senescence (Campisi and d'Adda di Fagagna, 2007). Also a marker and a mediator of senescence (Vaughan et al., 2017), the endothelial plasminogen activator inhibitor type-1 (SERPINE1), known as PAI-1, plays an essential role in radiation enteropathy (Milliat et al., 2008; Rannou et al., 2015). Involved in cell–cell interactions, cell adhesion, and migration, CD44 is upregulated in irradiated HUVECs, associated with radiation-induced senescence, and promotes cell adhesion in response to irradiation of endothelial cells (Kim et al., 2014; Lowe and Raj, 2014). Last, transgelin-2 (TAGLN2, also known as SM22-alpha, for smooth muscle 22-alpha) has been shown to be upregulated in endothelial cells that undergo endothelial-mesenchymal transition, a process that intersects with senescence (Mintet et al., 2015; Sasaki et al., 2020). On the other hand, the link between ionizing radiation and reticulon 4 (RTN4, also known as Nogo-B), which is a member of the reticulon protein family and an inducer of apoptosis in certain types of cancer cell (Kawaguchi et al., 2018; Li et al., 2001), is not documented.

Further, miRNAs are able to modulate the angiogenic properties of HUVECs (Poliseno et al., 2006) and are differentially expressed following radiation in endothelial cells (Wagner-Ecker et al., 2010). More generally, miRNAs are modulated in various cells, tissues, and fluids in response to ionizing radiation (Belli and Tabocchini, 2020; Metheetrairut and Slack, 2013). However, the roles of the 4 miRNAs we selected, i.e. miR10b, mi181a, miR181c, and miR5582, have never been established in endothelial cells in response to irradiation.

The local production of fumarate, defined as an oncometabolite, by fumarate hydratase has been characterized in cancer cells as a DNA repair factor required in nonhomologous end joining (Jiang et al., 2015; Yogev et al., 2010) and may have a direct role in checkpoint signaling (Johnson et al., 2018). Also, we identified AMP as an essential factor in the development of late dysfunction induced by irradiation. Cyclic adenosine monophosphate (cAMP) is the prototypical second messenger that is generated by adenylyl cyclase on stimulation of G protein–coupled receptors. cAMP exerts an inhibitory effect on DNA replication, leading to cell arrest in S phase (Naderi et al., 2005). The activation of cAMP signaling inhibits DNA damage-induced apoptosis through the DNA damage–induced accumulation of p53 (Naderi et al., 2009).

Angiogenesis, a function strongly altered by radiation, can be modified *in vitro*

Among the processes predicted by modeling and systems biology, angiogenesis is a key function that can be affected by ionizing radiation. Radiation therapy is considered to inhibit angiogenesis by damaging the endothelium (Fuks et al., 1992; Hatjikondi et al., 1996; Rose et al., 1999). However, there are also *in vivo* studies that show that ionizing radiation induces angiogenesis (Kaminski et al., 1978, 1983) and increases the expression of genes that favor it (Polytarchou et al., 2004), but no study explains these contradictory

effects. Irradiation has been shown *in vivo* to influence the expression, deposition, and turnover of extracellular matrix proteins in a way that secondarily promotes normal and tumor angiogenesis (Giannopoulou et al., 2001). These data indicate that radiation first inhibits angiogenesis and then indirectly stimulates angiogenesis through the necessary healing process that results from radiation-induced damage. Similarly, in this study, we observed that ionizing radiation inhibits the expression of proangiogenic genes and the formation of tubes formed by HUVECs on Matrigel, whereas, on the other hand, we showed that proangiogenic genes were stimulated in mice locally exposed to radiation. We modulated in HUVECs the expression of 5 entities highlighted by dynamic modeling to study their involvement in the alteration of tube formation after irradiation. Inhibition of the expression of SERPINE1, CD44, and CDKN2A was found to inhibit angiogenesis, even more so when the cells had undergone irradiation. This antiangiogenic effect was associated with the decrease in the expression of CD34, an essential key player in angiogenesis (Siemerink et al., 2012). Conversely, administration of miR181a and miR181c limited or even slightly counteracted the irradiation-induced inhibition of angiogenesis and stimulated the expression of proangiogenic genes. These validations confirmed that the best candidates obtained by our machine learning model were functionally modified in vascular endothelial cells with respect to angiogenesis after irradiation *in vitro*.

Conclusions

The strategy we present here facilitates unsupervised high-level feature extraction of important omics data to learn how ionizing-radiation-induced endothelial dysfunction may evolve over time. As a proof of principle, the experimental validation of such a dysfunction, here angiogenesis, allows us to propose new targets to restore impaired angiogenesis or inhibit neovascularization in growing tumors.

Limitations of the study

This study focused on identifying molecular pathways and target molecules involved in the initiation and development of ionizing-radiation-induced vascular endothelial dysfunction using large-scale omics analyses. For the transcriptomic study, we chose to target the analysis on genes of interest using premade TaqMan low-density 384-well arrays (TLDA) for human angiogenesis, inflammation, apoptosis, immune response, and protein kinase panels, representing approximately 400 genes, whereas the number of genes expressed and detected in HUVECs can be expected to average 1,500–2,500 genes per cell in sc-RNAseq experiments (Zirkel et al., 2018). Although this strategy represents an obvious advantage, as gene expression is measured with the robust RT-PCR technique, assessment of unmeasured gene expression levels may provide other interesting information that we will need to investigate in the future.

STAR★METHODS

Detailed methods are provided in the online version of this paper and include the following:

- KEY RESOURCES TABLE
- RESOURCE AVAILABILITY
  - Lead contact
  - Materials availability
  - Data and code availability
- EXPERIMENTAL MODEL AND SUBJECT DETAILS
  - Cells
  - Animals
- METHOD DETAILS
  - Irradiation procedure
  - Estimation of the number and volume of cells
  - RNA extraction
  - mRNA expression analysis
  - miRNA expression analysis
  - Protein expression analysis
  - Metabolite expression analysis
  - Omics data visualization and denoising
  - Construction of the irradiated complexes
  - Summary of the topological invariants in the datasets: barcodes landscapes and silhouettes
  - Mapping of topological invariants
  - Functional analysis of persistent candidates

- Integrated omics-graph construction
- Graph convolutional networks of integrated omics-graph
- siRNA and miRNA mimic transfection
- *In vitro* tube formation assay
- β-gal staining

- QUANTIFICATION AND STATISTICAL ANALYSIS

SUPPLEMENTAL INFORMATION

Supplemental information can be found online at https://doi.org/10.1016/j.isci.2021.103685.

ACKNOWLEDGMENTS

This work is supported by Electricité de France (Groupe Gestion Projet Radioprotection), the Institut de Radioprotection et de Sûreté Nucléaire (ROSIRIS program), INSERM, the University of Normandy-Rouen, the Region Normandie, and the European Union. Europe gets involved in Normandy with the European Regional Development Fund (ERDF). The funding agencies were not involved in any research plan relative to the study design, data collection and analysis, decision to publish, or drafting of the manuscript.

AUTHOR CONTRIBUTIONS

A.F., F.M., and O.G. conceived and designed the experiments. F.C., P.C., S. S., S.L., V.B., G.T., B.M., V.P., A.F., L.S., F.M., and O.G. performed experiments. I.M., G.T., and F.C. analyzed the miRNomic data. I.M., G.T., V.B., A.F., F.M., and O.G. analyzed the transcriptomic data. I.M., P.C., and D.V. analyzed the proteomic data. I.M., L.S., and J.C.M. analyzed the metabolomic data. I.M. performed formal analysis. I.M., P.C., L.S., J.C.M., and O.G. wrote the original manuscript. I.M., P.C., D.V., L.S., J.C.M., V.P., M.S, M.A.B., F.M., and O.G. reviewed and edited the manuscript. Funding acquisition was done by F.M. and O.G.; F.M. and O.G. supervised the project. All authors contributed to the manuscript.

DECLARATION OF INTERESTS

The authors declare no competing interests.

Received: August 1, 2021
Revised: October 4, 2021
Accepted: December 22, 2021
Published: January 21, 2022

REFERENCES

Adams, H., Vejdemo-Johansson, M., and Tausz, A. (2014). JavaPlex: a research software package for persistent (co)-homology. In Proceedings of ICMS, H. Hong and C. Yap, eds. (Springer), pp. 129–136.

Ashburner, M., Ball, C.A., Blake, J.A., Botstein, D., Butler, H., Cherry, J.M., Davis, A.P., Dolinski, K., Dwight, S.S., Eppig, J.T., et al. (2000). Gene ontology: tool for the unification of biology. The Gene Ontology Consortium. Nat. Genet. *25*, 25–29.

Azimzadeh, O., Sievert, W., Sarioglu, H., Merl-Pham, J., Yentrapalli, R., Bakshi, M.V., Janik, D., Ueffing, M., Atkinson, M.J., Multhoff, G., et al. (2015). Integrative proteomics and targeted transcriptomics analyses in cardiac endothelial cells unravel mechanisms of long-term radiation-induced vascular dysfunction. J. Proteome Res. *14*, 1203–1219.

Belli, M., and Tabocchini, M.A. (2020). Ionizing radiation-induced epigenetic modifications and their relevance to radiation protection. Int. J. Mol. Sci. *21*, 5993.

Ben Kacem, M., Benadjaoud, M.A., Dos Santos, M., Soysouvanh, F., Buard, V., Tarlet, G., Le Guen, B., Francois, A., Guipaud, O., Milliat, F., et al. (2020). Variation of 4 MV X-ray dose rate strongly impacts biological response both *in vitro* and *in vivo*. Sci. Rep. *10*, 7021.

Borsuk, K. (1948). On the imbedding of systems of compacta in simplicial complexes. Fund. Math. *35*, 217–234.

Brown, S., Banfill, K., Aznar, M.C., Whitehurst, P., and Faivre Finn, C. (2019). The evolving role of radiotherapy in non-small cell lung cancer. Br. J. Radiol. *92*, 20190524.

Bubenik, P. (2015). Statistical topological data analysis using persistence landscapes. J. Mach. Learn. Res. *16*, 77–102.

Campisi, J., and d'Adda di Fagagna, F. (2007). Cellular senescence: when bad things happen to good cells. Nat. Rev. Mol. Cell Biol. *8*, 729–740.

Carlsson, G.E., Zomorodian, A., Collins, A., and Guibas, L. (2005). Persistence barcodes for shapes. Int. J. Shape Model. *11*, 149–187.

Chambers, M.C., Maclean, B., Burke, R., Amodei, D., Ruderman, D.L., Neumann, S., Gatto, L., Fischer, B., Pratt, B., Egertson, J., et al. (2012). A cross-platform toolkit for mass spectrometry and proteomics. Nat. Biotechnol. *30*, 918–920.

Chazal, F., Fasy, B.T., Lecc, i.F., Rinaldo, A., and Wasserman, L. (2015). Stochastic convergence of persistence landscapes and silhouettes. J. Comput. Geom. *6*, 140–161.

Chen, S., and Mar, J.C. (2018). Evaluating methods of inferring gene regulatory networks highlights their lack of performance for single cell gene expression data. BMC Bioinf. *19*, 232.

Chou, C.H., Chen, S.U., and Cheng, J.C. (2009). Radiation-induced interleukin-6 expression through MAPK/p38/NF-kappaB signaling pathway and the resultant antiapoptotic effect on endothelial cells through Mcl-1 expression with sIL6-Ralpha. Int. J. Radiat. Oncol. Biol. Phys. *75*, 1553–1561.

Christersdottir, T., Pirault, J., Gistera, A., Bergman, O., Gallina, A.L., Baumgartner, R.,

Lundberg, A.M., Eriksson, P., Yan, Z.Q., Paulsson-Berne, G., et al. (2019). Prevention of radiotherapy-induced arterial inflammation by interleukin-1 blockade. Eur. Heart J. *40*, 2495–2503.

Corre, I., Niaudet, C., and Paris, F. (2010). Plasma membrane signaling induced by ionizing radiation. Mutat. Res. *704*, 61–67.

Cruchant, O. (2020). Faster, Cheaper, Leaner: Improving Real-Time ML Inference Using Apache MXNet (The Apache Software Foundation). https://medium.com/apache-mxnet/faster-cheaper-leaner-improving-real-time-ml-inference-using-apache-mxnet-2ee245668b55.

Defferrard, M., Bresson, X., and Vandergheynst, P. (2016). Convolutional neural networks on graphs with fast localised spectral filtering. Adv. Neural Inf. Process. Syst. *29*, 3844–3852.

Ding, M., Tang, J., and Zhang, J. (2018). Semi-supervised learning on graphs with generative adversarial nets. In CIKM '18: Proceedings of the 27th ACM International Conference on Information and Knowledge (): ACM), pp. 313–322.

Eraslan, G., Avsec, Z., Gagneur, J., and Theis, F.J. (2019). Deep learning: new computational modelling techniques for genomics. Nat. Rev. Genet. *20*, 389–403.

Fasy, B.T., Kim, J., Lecci, F., Maria, C., Millman, D.L., and Rouvreau, V. (2019). TDA: Statistical Tools for Topological Data Analysis (CRAN-R repository). https://cran.r-project.org/web/packages/TDA/index.html.

Fuks, Z., Vlodavsky, I., Andreeff, M., McLoughlin, M., and Haimovitz-Friedman, A. (1992). Effects of extracellular matrix on the response of endothelial cells to radiation *in vitro*. Eur. J. Cancer *28A*, 725–731.

Giacomoni, F., Le Corguille, G., Monsoor, M., Landi, M., Pericard, P., Petera, M., Duperier, C., Tremblay-Franco, M., Martin, J.F., Jacob, D., et al. (2015). Workflow4Metabolomics: a collaborative research infrastructure for computational metabolomics. Bioinformatics *31*, 1493–1495.

Giannopoulou, E., Katsoris, P., Hatziapostolou, M., Kardamakis, D., Kotsaki, E., Polytarchou, C., Parthymou, A., Papaioannou, S., and Papadimitriou, E. (2001). X-rays modulate extracellular matrix *in vivo*. Int. J. Cancer *94*, 690–698.

Guipaud, O., Jaillet, C., Clement-Colmou, K., Francois, A., Supiot, S., and Milliat, F. (2018). The importance of the vascular endothelial barrier in the immune-inflammatory response induced by radiotherapy. Br. J. Radiol. *91*, 20170762.

Halle, M., Ekstrom, M., Farnebo, F., and Tornvall, P. (2010a). Endothelial activation with prothrombotic response in irradiated microvascular recipient veins. J. Plast. Reconstr. Aesthet. Surg. *63*, 1910–1916.

Halle, M., Gabrielsen, A., Paulsson-Berne, G., Gahm, C., Agardh, H.E., Farnebo, F., and Tornvall, P. (2010b). Sustained inflammation due to nuclear factor-kappa B activation in irradiated human arteries. J. Am. Coll. Cardiol. *55*, 1227–1236.

Hamilton, W.L., Ying, R., and Leskovec, J. (2017a). Inductive representation learning on large graphs. arXiv preprint. https://arxiv.org/abs/1609.02907v4.

Hamilton, W.L., Ying, R., and Leskovec, J. (2017b). Representation learning on graphs: methods and applications. arXiv preprint. https://arxiv.org/abs/1709.05584v3.

Hatjikondi, O., Ravazoula, P., Kardamakis, D., Dimopoulos, J., and Papaioannou, S. (1996). *In vivo* experimental evidence that the nitric oxide pathway is involved in the X-ray-induced antiangiogenicity. Br. J. Cancer *74*, 1916–1923.

Hauer-Jensen, M., Denham, J.W., and Andreyev, H.J. (2014). Radiation enteropathy–pathogenesis, treatment and prevention. Nat. Rev. Gastroenterol. Hepatol. *11*, 470–479.

Hauer-Jensen, M., Poulakos, L., and Osborne, J.W. (1988). Effects of accelerated fractionation on radiation injury of the small intestine: a new rat model. Int. J. Radiat. Oncol. Biol. Phys. *14*, 1205–1212.

Hauer-Jensen, M., Poulakos, L., and Osborne, J.W. (1990). Intestinal complications following accelerated fractionated x-irradiation. An experimental study in the rat. Acta Oncol. *29*, 229–234.

Hauer-Jensen, M., Sauer, T., Devik, F., and Nygaard, K. (1983). Late changes following single dose roentgen irradiation of rat small intestine. Acta Radiol. Oncol. *22*, 299–303.

Haug, K., Cochrane, K., Nainala, V.C., Williams, M., Chang, J., Jayaseelan, K.V., and O'Donovan, C. (2020). MetaboLights: a resource evolving in response to the needs of its scientific community. Nucleic Acids Res. *48*, D440–D444.

Hausmann, J.C. (1995). On the Vietoris-Rips complexes and a cohomology theory for metric spaces. Ann. Math. Stud. *138*, 175–188.

Heinonen, M., Guipaud, O., Milliat, F., Buard, V., Micheau, B., Tarlet, G., Benderitter, M., Zehraoui, F., and d'Alche-Buc, F. (2015). Detecting time periods of differential gene expression using Gaussian processes: an application to endothelial cells exposed to radiotherapy dose fraction. Bioinformatics *31*, 728–735.

Heinonen, M., Milliat, F., Benadjaoud, M.A., Francois, A., Buard, V., Tarlet, G., d'Alche-Buc, F., and Guipaud, O. (2018). Temporal clustering analysis of endothelial cell gene expression following exposure to a conventional radiotherapy dose fraction using Gaussian process clustering. PLoS One *13*, e0204960.

Herskind, C., Talbot, C.J., Kerns, S.L., Veldwijk, M.R., Rosenstein, B.S., and West, C.M. (2016). Radiogenomics: a systems biology approach to understanding genetic risk factors for radiotherapy toxicity? Cancer Lett. *382*, 95–109.

Jaillet, C., Morelle, W., Slomianny, M.C., Paget, V., Tarlet, G., Buard, V., Selbonne, S., Caffin, F., Rannou, E., Martinez, P., et al. (2017). Radiation-induced changes in the glycome of endothelial cells with functional consequences. Sci. Rep. *7*, 5290.

Jiang, Y., Qian, X., Shen, J., Wang, Y., Li, X., Liu, R., Xia, Y., Chen, Q., Peng, G., Lin, S.Y., et al. (2015). Local generation of fumarate promotes DNA repair through inhibition of histone H3 demethylation. Nat. Cell Biol. *17*, 1158–1168.

Johnson, T.I., Costa, A.S.H., Ferguson, A.N., and Frezza, C. (2018). Fumarate hydratase loss promotes mitotic entry in the presence of DNA damage after ionising radiation. Cell Death Dis. *9*, 913.

Kaminski, M., Majewski, S., Kaminska, G., Bem, W., and Szmurlo, A. (1978). Enhancing effect of X-ray irradiation on a new blood vessel formation in mice tested by lymphocyte induced angiogenesis assay. Arch. Immunol. Ther. Exp. *26*, 1075–1078.

Kaminski, M.J., Majewski, S., Kaminska, G., Bem, W., and Szmurlo, A. (1983). Protease-mediated enhancement of lymphocyte-induced angiogenesis in X-ray irradiated mice. Int. J. Radiat. Biol. Relat. Stud. Phys. Chem. Med. *43*, 149–156.

Kawaguchi, N., Tashiro, K., Taniguchi, K., Kawai, M., Tanaka, K., Okuda, J., Hayashi, M., and Uchiyama, K. (2018). Nogo-B (Reticulon-4B) functions as a negative regulator of the apoptotic pathway through the interaction with c-FLIP in colorectal cancer cells. Biochim. Biophys. Acta Mol. Basis Dis. *1864*, 2600–2609.

Kim, K.S., Kim, J.E., Choi, K.J., Bae, S., and Kim, D.H. (2014). Characterization of DNA damage-induced cellular senescence by ionizing radiation in endothelial cells. Int. J. Radiat. Biol. *90*, 71–80.

Kipf, T.N., and Welling, M. (2016). Semi-supervised classification with graph convolutional networks. arXiv preprint. https://arxiv.org/abs/1609.02907v4.

Knyazev, B., Lin, X., Amer, M.R., and Taylor, G.W. (2018). Spectral multigraph networks for discovering and fusing relationships in molecules. arXiv preprint. https://arxiv.org/abs/1811.09595.

Korbel, F. (2012). FFmpeg Basics: Multimedia Handling with a Fast Audio and Video Encoder (CreateSpace Independent Publishing Platform)).

Korpela, E., and Liu, S.K. (2014). Endothelial perturbations and therapeutic strategies in normal tissue radiation damage. Radiat. Oncol. *9*, 266.

Lafargue, A., Degorre, C., Corre, I., Alves-Guerra, M.C., Gaugler, M.H., Vallette, F., Pecqueur, C., and Paris, F. (2017). Ionizing radiation induces long-term senescence in endothelial cells through mitochondrial respiratory complex II dysfunction and superoxide generation. Free Radic. Biol. Med. *108*, 750–759.

Langberg, C.W., Sauer, T., Reitan, J.B., and Hauer-Jensen, M. (1992). Tolerance of rat small intestine to localized single dose and fractionated irradiation. Acta Oncol. *31*, 781–787.

Lauwers, O., and De Moor, B. (2017). A time series distance measure for efficient clustering of input/output signals by their underlying dynamics. IEEE Control Syst. Lett. *1*, 286–291.

Lees, J.G., Heriche, J.K., Morilla, I., Fernandez, J.M., Adler, P., Krallinger, M., Vilo, J., Valencia, A., Ellenberg, J., Ranea, J.A., et al. (2015). FUN-L: gene prioritization for RNAi screens. Bioinformatics *31*, 2052–2053.

Leonawicz, M. (2017). Mapmate. https://github.com/leonawicz/mapmate.

Li, Q., Qi, B., Oka, K., Shimakage, M., Yoshioka, N., Inoue, H., Hakura, A., Kodama, K., Stanbridge, E.J., and Yutsudo, M. (2001). Link of a new type of apoptosis-inducing gene ASY/Nogo-B to human cancer. Oncogene *20*, 3929–3936.

Lloyd, S.P. (1982). Least squares quantization in PCM. IEEE Trans. Inf. Theor. *28*, 129–137.

Lo, S.S., Fakiris, A.J., Chang, E.L., Mayr, N.A., Wang, J.Z., Papiez, L., Teh, B.S., McGarry, R.C., Cardenes, H.R., and Timmerman, R.D. (2010). Stereotactic body radiation therapy: a novel treatment modality. Nat. Rev. Clin. Oncol. *7*, 44–54.

Lowe, D., and Raj, K. (2014). Premature aging induced by radiation exhibits pro-atherosclerotic effects mediated by epigenetic activation of CD44 expression. Aging Cell *13*, 900–910.

Mestdagh, P., Van Vlierberghe, P., De Weer, A., Muth, D., Westermann, F., Speleman, F., and Vandesompele, J. (2009). A novel and universal method for microRNA RT-qPCR data normalization. Genome Biol. *10*, R64.

Metheetrairut, C., and Slack, F.J. (2013). MicroRNAs in the ionizing radiation response and in radiotherapy. Curr. Opin. Genet. Dev. *23*, 12–19.

Mi, H., Muruganujan, A., Ebert, D., Huang, X., and Thomas, P.D. (2019). PANTHER version 14: more genomes, a new PANTHER GO-slim and improvements in enrichment analysis tools. Nucleic Acids Res. *47*, D419–D426.

Milliat, F., Sabourin, J.C., Tarlet, G., Holler, V., Deutsch, E., Buard, V., Tamarat, R., Atfi, A., Benderitter, M., and Francois, A. (2008). Essential role of plasminogen activator inhibitor type-1 in radiation enteropathy. Am. J. Pathol. *172*, 691–701.

Mintet, E., Rannou, E., Buard, V., West, G., Guipaud, O., Tarlet, G., Sabourin, J.C., Benderitter, M., Fiocchi, C., Milliat, F., et al. (2015). Identification of endothelial-to-mesenchymal transition as a potential participant in radiation proctitis. Am. J. Pathol. *185*, 2550–2562.

Molla, M., Panes, J., Casadevall, M., Salas, A., Conill, C., Biete, A., Anderson, D.C., Granger, D.N., and Pique, J.M. (1999). Influence of dose-rate on inflammatory damage and adhesion molecule expression after abdominal radiation in the rat. Int. J. Radiat. Oncol. Biol. Phys. *45*, 1011–1018.

Morilla, I., Doblas, S., Garteiser, P., Zappa, M., and Ogier-Denis, E. (2017). Scores of intestinal fibrosis from wavelet-based magnetic resonance imaging models. In Bioinform Biomed Eng, I. Rojas and F. Ortuño, eds. (Springer), pp. 569–578.

Morilla, I., and Ranea, J.A. (2017). Mathematical deconvolution uncovers the genetic regulatory signal of cancer cellular heterogeneity on resistance to paclitaxel. Mol. Genet. Genom. *292*, 857–869.

Munch, E. (2017). A user's guide to topological data analysis. J. Learn. Analytics *4*, 47–61.

Naderi, E.H., Findley, H.W., Ruud, E., Blomhoff, H.K., and Naderi, S. (2009). Activation of cAMP signaling inhibits DNA damage-induced apoptosis in BCP-ALL cells through abrogation of p53 accumulation. Blood *114*, 608–618.

Naderi, S., Wang, J.Y., Chen, T.T., Gutzkow, K.B., and Blomhoff, H.K. (2005). cAMP-mediated inhibition of DNA replication and S phase progression: involvement of Rb, p21Cip1, and PCNA. Mol. Biol. Cell *16*, 1527–1542.

Nikitin, A., Egorov, S., Daraselia, N., and Mazo, I. (2003). Pathway studio–the analysis and navigation of molecular networks. Bioinformatics *19*, 2155–2157.

Oudot, S.Y. (2015). Persistence Theory: From Quiver Representations to Data Analysis (American Mathematical Society).

Paget, V., Ben Kacem, M., Dos Santos, M., Benadjaoud, M.A., Soysouvanh, F., Buard, V., Georges, T., Vaurijoux, A., Gruel, G., Francois, A., et al. (2019). Multiparametric radiobiological assays show that variation of X-ray energy strongly impacts relative biological effectiveness: comparison between 220 kV and 4 MV. Sci. Rep. *9*, 14328.

Perez-Riverol, Y., Csordas, A., Bai, J., Bernal-Llinares, M., Hewapathirana, S., Kundu, D.J., Inuganti, A., Griss, J., Mayer, G., Eisenacher, M., et al. (2019). The PRIDE database and related tools and resources in 2019: improving support for quantification data. Nucleic Acids Res. *47*, D442–D450.

Poliseno, L., Tuccoli, A., Mariani, L., Evangelista, M., Citti, L., Woods, K., Mercatanti, A., Hammond, S., and Rainaldi, G. (2006). MicroRNAs modulate the angiogenic properties of HUVECs. Blood *108*, 3068–3071.

Polytarchou, C., Gligoris, T., Kardamakis, D., Kotsaki, E., and Papadimitriou, E. (2004). X-rays affect the expression of genes involved in angiogenesis. Anticancer Res. *24*, 2941–2945.

Qiu, B., Aili, A., Xue, L., Jiang, P., and Wang, J. (2020). Advances in radiobiology of stereotactic ablative radiotherapy. Front. Oncol. *10*, 1165.

Rannou, E., Francois, A., Toullec, A., Guipaud, O., Buard, V., Tarlet, G., Mintet, E., Jaillet, C., Iruela-Arispe, M.L., Benderitter, M., et al. (2015). *In vivo* evidence for an endothelium-dependent mechanism in radiation-induced normal tissue injury. Sci. Rep. *5*, 15738.

Raudvere, U., Kolberg, L., Kuzmin, I., Arak, T., Adler, P., Peterson, H., and Vilo, J. (2019). g:Profiler: a web server for functional enrichment analysis and conversions of gene lists (2019 update). Nucleic Acids Res. *47*, W191–W198.

Rhee, S., Seo, S., and Kim, S. (2018). Hybrid approach of relation network and localized graph convolutional filtering for breast cancer subtype classification. arXiv preprint. https://arxiv.org/abs/1711.05859.

Rochat, B. (2017). Proposed confidence scale and ID score in the identification of known-unknown compounds using high resolution MS data. J. Am. Soc. Mass Spectrom. *28*, 709–723.

Rose, R.W., Grant, D.S., O'Hara, M.D., and Williamson, S.K. (1999). The role of laminin-1 in the modulation of radiation damage in endothelial cells and differentiation. Radiat. Res. *152*, 14–28.

Sasaki, N., Itakura, Y., and Toyoda, M. (2020). Rapamycin promotes endothelial-mesenchymal transition during stress-induced premature senescence through the activation of autophagy. Cell Commun. Signal. *18*, 43.

Schwacke, J.H., Hill, E.G., Krug, E.L., Comte-Walters, S., and Schey, K.L. (2009). iQuantitator: a tool for protein expression inference using iTRAQ. BMC Bioinf. *10*, 342.

Scoville, N.A. (2019). Discrete Morse Theory (American Mathematical Society).

Siemerink, M.J., Klaassen, I., Vogels, I.M., Griffioen, A.W., Van Noorden, C.J., and Schlingemann, R.O. (2012). CD34 marks angiogenic tip cells in human vascular endothelial cell cultures. Angiogenesis *15*, 151–163.

Simone, C.B., 2nd, Wildt, B., Haas, A.R., Pope, G., Rengan, R., and Hahn, S.M. (2013). Stereotactic body radiation therapy for lung cancer. Chest *143*, 1784–1790.

Singh, G., Memoli, F., and Carlsson, G.E. (2007). Topological methods for the analysis of high dimensional data sets and 3D object recognition. In Eurographics Symposium on Point-Based Graphics, M. Botsch, R. Pajarola, B. Chen, and M. Zwicker, eds.) (The Eurographics Association), pp. 91–100.

Soysouvanh, F., Benadjaoud, M.A., Dos Santos, M., Mondini, M., Lavigne, J., Bertho, A., Buard, V., Tarlet, G., Adnot, S., Deutsch, E., et al. (2020). Stereotactic lung irradiation in mice promotes long-term senescence and lung injury. Int. J. Radiat. Oncol. Biol. Phys. *106*, 1017–1027.

Stillwell, J. (1993). Classical Topology and Combinatorial Group Theory (Springer-Verlag New York).

Tauzin, G., Lupo, U., Tunstall, L., Burella Pérez, J., Caorsi, M., Reise, W., Medina-Mardones, A., Dassatti, A., and Hess, K. (2020). Giotto-Tda: a topological data analysis toolkit for machine learning and data exploration. arXiv preprint. https://arxiv.org/abs/2004.02551.

Toullec, A., Buard, V., Rannou, E., Tarlet, G., Guipaud, O., Robine, S., Iruela-Arispe, M.L., Francois, A., and Milliat, F. (2018). HIF-1alpha deletion in the endothelium, but not in the epithelium, protects from radiation-induced enteritis. Cell. Mol. Gastroenterol. Hepatol. *5*, 15–30.

van der Kloet, F.M., Bobeldijk, I., Verheij, E.R., and Jellema, R.H. (2009). Analytical error reduction using single point calibration for accurate and precise metabolomic phenotyping. J. Proteome Res. *8*, 5132–5141.

van der Maaten, L.J.P., and Hinton, G.E. (2008). Visualizing data using t-SNE. J. Mach Learn. Res. *9*, 2579–2605.

van Veen, H.J., and Saul, N. (2019). KeplerMapper. https://doi.org/10.5281/zenodo.1054444.

Vaughan, D.E., Rai, R., Khan, S.S., Eren, M., and Ghosh, A.K. (2017). Plasminogen activator inhibitor-1 is a marker and a mediator of senescence. Arterioscler. Thromb. Vasc. Biol. *37*, 1446–1452.

Vlachos, I.S., Kostoulas, N., Vergoulis, T., Georgakilas, G., Reczko, M., Maragkakis, M., Paraskevopoulou, M.D., Prionidis, K., Dalamagas, T., and Hatzigeorgiou, A.G. (2012). DIANA miRPath v.2.0: investigating the combinatorial effect of microRNAs in pathways. Nucleic Acids Res. *40*, W498–W504.

Wagner-Ecker, M., Schwager, C., Wirkner, U., Abdollahi, A., and Huber, P.E. (2010). MicroRNA expression after ionizing radiation in human endothelial cells. Radiat. Oncol. *5*, 25.

Warde-Farley, D., Donaldson, S.L., Comes, O., Zuberi, K., Badrawi, R., Chao, P., Franz, M., Grouios, C., Kazi, F., Lopes, C.T., et al. (2010). The GeneMANIA prediction server: biological network integration for gene prioritization and predicting gene function. Nucleic Acids Res. *38*, W214–W220.

Wijerathne, H., Langston, J.C., Yang, Q., Sun, S., Miyamoto, C., Kilpatrick, L.E., and Kiani, M.F. (2021). Mechanisms of radiation-induced endothelium damage: emerging models and technologies. Radiother. Oncol. *158*, 21–32.

Wishart, D.S., Feunang, Y.D., Marcu, A., Guo, A.C., Liang, K., Vazquez-Fresno, R., Sajed, T., Johnson, D., Li, C., Karu, N., et al. (2018). HMDB 4.0: the human metabolome database for 2018. Nucleic Acids Res. *46*, D608–D617.

Yogev, O., Singer, E., Shaulian, E., Goldberg, M., Fox, T.D., and Pines, O. (2010). Fumarase: a mitochondrial metabolic enzyme and a cytosolic/nuclear component of the DNA damage response. PLoS Biol. *8*, e1000328.

Zheng, H., Wang, J., Koteliansky, V.E., Gotwals, P.J., and Hauer-Jensen, M. (2000). Recombinant soluble transforming growth factor beta type II receptor ameliorates radiation enteropathy in mice. Gastroenterology *119*, 1286–1296.

Zirkel, A., Nikolic, M., Sofiadis, K., Mallm, J.P., Brackley, C.A., Gothe, H., Drechsel, O., Becker, C., Altmuller, J., Josipovic, N., et al. (2018). HMGB2 loss upon senescence entry disrupts genomic organization and induces CTCF clustering across cell types. Mol. Cell *70*, 730–744.e736.

Zitvogel, L., and Kroemer, G. (2015). Subversion of anticancer immunosurveillance by radiotherapy. Nat. Immunol. *16*, 1005–1007.

Zomorodian, A., and Carlsson, G.E. (2004). Computing persistent homology. Discrete Comput. Geom. *33*, 249–274.

STAR★METHODS

KEY RESOURCES TABLE

REAGENT or RESOURCE	SOURCE	IDENTIFIER
Chemicals, peptides, and recombinant proteins		
Dulbecco's Phosphate Buffered Saline	Thermo Fisher Scientific	Cat#: 14190-094
mirVana™ miRNA Isolation kit	Thermo Fisher Scientific	Cat#: AM1560
RNeasy Mini Kit	Qiagen	Cat#: 74104
EBM-2, Endothelial Cell Basal Medium-2	Lonza	Cat#: CC-3156
Trypsin-EDTA	Thermo Fisher Scientific	Cat#: 25300054
Trypan blue dye	Bio-Rad	Cat#: 145-0013
Dharmafect 1, Transfection Reagent	Thermo Fisher Scientific	Cat#: T-2001-02
Nuclease-free water	Qiagen	Cat#: 129114
Gibco™ Opti-MEM™ I Reduced Serum Medium	Thermo Fisher Scientific	Cat#: 31985-065
BD Matrigel Basement Membrane Matrix	BD Biosciences	Cat#: 354234
AErrane (Isoflurane)	Abbot GmbH	Cat#: DDG9623
High-Capacity cDNA Reverse Transcription Kit	Thermo Fisher Scientific	Cat#: 4368814
Ethanol absolute	VWR	Cat#: 20821.365
TaqMan™ Fast Universal PCR Master Mix (2X), no AmpErase™ UNG	Thermo Fisher Scientific	Cat#: 4366072
TaqMan™ Gene Expression Master Mix	Thermo Fisher Scientific	Cat#: 4370074
Megaplex™ RT Primers, Human Pool Set v3.0	Thermo Fisher Scientific	Cat#: 4444745
TaqMan™ PreAmp Master Mix	Thermo Fisher Scientific	Cat#: 4391128
Bicinchoninic Acid (BCA) Kit for Protein Determination	Sigma-Aldrich	Cat#: BCA1-1KT
Urea	Sigma-Aldrich	Cat#: 51456
Triethylammonium bicarbonate buffer	Thermo Fisher Scientific	Cat#: 15215753
cOmplete™, Mini, EDTA-free Protease Inhibitor Cocktail	Sigma-Aldrich	Cat#: 11836170001
ProteaseMAX™ Surfactant, Trypsin Enhancer	Promega	Cat#: V2071
Tris(2-carboxyethyl)phosphine hydrochloride	Sigma-Aldrich	Cat#: 75259
Iodoaceatmide	Sigma-Aldrich	Cat#: I1149
Sequencing Grade Modified Trypsin	Promega	Cat#: V5111
iTRAQ® Reagents Multiplex Kit	SCIEX	Cat#: 4352135
3100 OFFGEL Fractionator High Res Kit, pH 3-10	Agilent	Cat#: 5188-6424
Acetonitrile	Sigma-Aldrich	Cat#: 34851
Formic acid	Sigma-Aldrich	Cat#: 695076
Methanol	Sigma-Aldrich	Cat#: 179337
β-Gal Staining Kit	Thermo Fischer Scientific	Cat#: K146501

(*Continued on next page*)

Continued

REAGENT or RESOURCE	SOURCE	IDENTIFIER
Critical commercial assays		
TaqMan™ Array Human Immune Panel	Thermo Fisher Scientific	Cat#: 4370499
TaqMan™ Array Human Protein Kinase Panel	Thermo Fisher Scientific	Cat#: 4365299
TaqMan™ Array Human Apoptosis Panel	Thermo Fisher Scientific	Cat#: 4378716
TaqMan™ Array Human Inflammation Panel	Thermo Fisher Scientific	Cat#: 4378722
TaqMan™ Array Human Angiogenesis Panel	Thermo Fisher Scientific	Cat#: 4378725
TaqMan™ Array Human MicroRNA A+B Cards Set v3.0	Thermo Fisher Scientific	Cat#: 4444913
Custom TaqMan® Array Human MicroRNA Cards	Thermo Fisher Scientific	Cat#: 4342265
Deposited data		
Raw proteomics data	This paper	PRIDE: PXD030572
Raw metabolomics data	This paper	MetaboLights: MTBLS3680
SWISS-PROT protein sequence database (release 20170315)	Uniprot	https://www.uniprot.org/
Mammal (Anatomy; CellEffect™; DiseaseFx®; GeneticVariant; Viruses) version 12.4.0.3 (Updated April 25, 2021) database from Elsevier	Elsevier	www.elsevier.com/pathway-studio
Human metabolome database (HMDB)		https://hmdb.ca/
Experimental models: Cell lines		
HUVEC – Human Umbilical Vein Endothelial Cells	Lonza	Cat#: C2519A
Experimental models: Organisms/strains		
C57BL/6J mouse	Charles River	Cat#: 000664
Oligonucleotides		
Primers for TaqMan® Human gene expression assay: SERPINE1 - Assay ID: Hs01126606_m1	Thermo Fisher Scientific	Cat#: 4331182
Primers for TaqMan® Human gene expression assay: CD44 - Assay ID: Hs01075861_m1	Thermo Fisher Scientific	Cat#: 4331182
Primers for TaqMan® Human gene expression assay: CDKN2A - Assay ID: Hs00924091_m1	Thermo Fisher Scientific	Cat#: 4331182
Primers for TaqMan® Human gene expression assay: CD34 - Assay ID: Hs00990732_m1	Thermo Fisher Scientific	Cat#: 4331182
Primers for TaqMan® Human gene expression assay: COL4A2 - Assay ID: Hs01098873_m1	Thermo Fisher Scientific	Cat#: 4331182
Primers for TaqMan® Human gene expression assay: IL6 - Assay ID: Hs00174131_m1	Thermo Fisher Scientific	Cat#: 4331182

(*Continued on next page*)

Continued

REAGENT or RESOURCE	SOURCE	IDENTIFIER
Primers for TaqMan® Human gene expression assay: PDGFRA - Assay ID: Hs00998018_m1	Thermo Fisher Scientific	Cat#: 4331182
Primers for TaqMan® Human gene expression assay: TIMP3 - Assay ID: Hs00165949_m1	Thermo Fisher Scientific	Cat#: 4331182
Primers for TaqMan® Human gene expression assay: VEGFA - Assay ID: Hs00900055_m1	Thermo Fisher Scientific	Cat#: 4331182
Primers for TaqMan® Human gene expression assay: ACTB - Assay ID: Hs99999903_m1	Thermo Fisher Scientific	Cat#: 4331182
Primers for TaqMan® Human/Mouse miRNA expression assay: miR181a-5p - Assay ID: 000480	Thermo Fisher Scientific	Cat#: 4427975
Primers for TaqMan® Human/Mouse miRNA expression assay: miR181c-5p - Assay ID: 000482	Thermo Fisher Scientific	Cat#: 4427975
Primers for TaqMan® Human/Mouse miRNA expression assay: U6 snRNA - Assay ID: 001973	Thermo Fisher Scientific	Cat#: 4427975
Primers for TaqMan® Mouse gene expression assay: SERPINE1 - Assay ID: Mm00437306_m1	Thermo Fisher Scientific	Cat#: 4331182
Primers for TaqMan® Mouse gene expression assay: ANGPT1 - Assay ID: Mm00456503_m1	Thermo Fisher Scientific	Cat#: 4331182
Primers for TaqMan® Mouse gene expression assay: ANGPTL1 - Assay ID: Mm01291815_m1	Thermo Fisher Scientific	Cat#: 4331182
Primers for TaqMan® Mouse gene expression assay: IL6 - Assay ID: Hs00174131_m1	Thermo Fisher Scientific	Cat#: 4331182
Primers for TaqMan® Mouse gene expression assay: MMP2 - Assay ID: Hs01548727_m1	Thermo Fisher Scientific	Cat#: 4331182
Non targeting siRNA	GE Healthcare	Cat#: D-001810-10-20
siRNA against human SERPINE1	GE Healthcare	Cat#: L-019376-01-0050
siRNA against human CD44	GE Healthcare	Cat#: L-009999-00-0020
siRNA against human CDKN2A	GE Healthcare	Cat#: L-011007-00-0020
Human miR181a-5p Mimic	Thermo Fisher Scientific	Cat#: MC10421
Human miR181c-5p Mimic	Thermo Fisher Scientific	Cat#: MC10181
miRIDIAN microRNA Mimic Transfection Control with Dy547	Thermo Fisher Scientific	Cat#: CP-004500-01-05
Software and algorithms		
Spectrum Mill, Rev B.04.00.127	Agilent Technologies	Cat#: G2721AA/G2733AA
R software	www.r-project.org	www.r-project.org
iQuantitator	Schwacke et al., 2009	https://bmcbioinformatics.biomedcentral.com/articles/10.1186/1471-2105-10-342#Sec17

(*Continued on next page*)

Continued

REAGENT or RESOURCE	SOURCE	IDENTIFIER
Chromeleon 6.8 software	Thermo Fisher Scientific	Cat#: CHROMELEON6
Xcalibur 3.0.63	Thermo Fisher Scientific	Cat#: XCALI-97553
ProteoWizard	Chambers et al., 2012	http://proteowizard.sourceforge.net/
van der Kloet algorithm	van der Kloet et al., 2009	https://pubs.acs.org/doi/abs/10.1021/pr900499r
Workflow4Metabolomics	Giacomoni et al., 2015	https://workflow4metabolomics.org
Pathway Studio Web Mammal version 12.4.0.3	Nikitin et al., 2003	www.elsevier.com/pathway-studio
DIANA Tools	Vlachos et al., 2012	http://diana.imis.athena-innovation.gr/DianaTools/
Topological Data Analysis version 1.6.9	Fasy et al., 2019	https://cran.r-project.org/web/packages/TDA/index.html
DataAssis software version 3.01	Thermo Fisher Scientific	https://www.thermofisher.com/
GraphPad Prism version 8.1.1	GraphPad Software	www.graphpad.com
ImageJ version 1.52a software	National Institutes of Health	http://imagej.nih.gov/ij
Other		
Gene Ontology resource	Ashburner et al., 2000	http://geneontology.org/
PANTHER classification resource version 14	Mi et al., 2019	http://pantherdb.org/
g:Profiler	Raudvere et al., 2019	https://biit.cs.ut.ee/gprofiler/
GeneMANIA	Warde-Farley et al., 2010	https://genemania.org/
JavaPlex	Adams et al., 2014	http://appliedtopology.github.io/javaplex/
FFmpeg function	Korbel, 2012	http://ffmpeg.org/
R package mapmate	Leonawicz, 2017	https://github.com/leonawicz/mapmate
Keplermapper	van Veen and Saul, 2019	http://doi.org/10.5281/zenodo.1054444
Angiogenesis Analyzer plugin for Image J	http://image.bio.methods.free.fr/ImageJ/?Angiogenesis-Analyzer-for-ImageJ	https://imagej.nih.gov/ij/macros/toolsets/

RESOURCE AVAILABILITY

Lead contact

Further information and requests for resources and reagents should be directed to and will be fulfilled by the lead contact, Olivier Guipaud (olivier.guipaud@irsn.fr).

Materials availability

This study did not generate new unique reagents.

Data and code availability

- The mass spectrometry proteomics data have been deposited to the ProteomeXchange Consortium via the PRIDE (Perez-Riverol et al., 2019) partner repository with accession number PRIDE: PXD030572. The mass spectrometry metabolomics data have been deposited at the MetaboLights database (Haug et al., 2020) with accession number MetaboLights: MTBLS3680. Both datasets are publicly available as of the date of publication. Accession numbers are listed in the key resources table. Raw data from real-time quantitative PCR and microscopy data reported in this paper will be shared by the lead contact upon request. The miRNA, mRNA, proteome and metabolome processed data reported in this study are supplied as Data S1, S2, S3, and S4.

- This paper does not report original code.
- Any additional information required to reanalyze the data reported in this paper is available from the lead contact upon request.

EXPERIMENTAL MODEL AND SUBJECT DETAILS

Cells

Human umbilical vein endothelial cells (HUVECs, pooled donors, newborn, male/female mixed, product code C2519A, batch number 0000465419) from Lonza were grown at 37°C with 5% CO_2 in EBM-2 MV medium containing 5% FBS (Lonza). Cells were authenticated by the suppliers and tested negative for mycoplasma, bacteria, yeast, and fungi, as guaranteed by the suppliers.

Animals

Male C57BL/6 mice came from Charles River Laboratories and were 10 weeks of age upon arrival. Animals were housed at the IRSN animal facilities authorized by the French Ministry of Agriculture for performing experiments on rodents. Animal experiments were performed in strict compliance with French and European guidelines and regulations on the protection of animals used for scientific purposes (EC Directive, 2010/63/EU and French Decree No. 2013–118). They were approved by IRSN's Animal Experimentation Ethics Committee, registered under number 81 and authorized by the French Ministry of Research under reference APAFIS#6209-2016072213325989 v2 (internal project number P15-04).

METHOD DETAILS

Irradiation procedure

Irradiation of HUVECs at a single dose of 20 Gy was performed using a ^{137}Cs source (IBL 637, CisBio, 1 $Gy.min^{-1}$). Non-irradiated cells (control samples) were left for the same amount of time on a benchtop near the irradiation room. All irradiations were carried out at 90–100% cell confluence and the same number of population doublings (passage 3, corresponding to 9 to 12 population doublings). The cells were collected at 0.5, 1, 2, 3, 4, 7, 14 and 21 days after irradiation or without having been irradiated (control samples) in order to prepare proteins (4 replicates per dose and per time point), mRNAs (3 replicates per dose and per time point), miRNA (3 replicates per dose and per time point) and metabolites (5 replicates per dose and per time point). For long-term experiments (14- and 21-days post-irradiation), the culture medium was changed every week.

Radiation enteropathy was induced by exposure of an intestinal segment to a single dose of 19 Gy (Milliat et al., 2008). Briefly, mice were anesthetized by spontaneous inhalation of isoflurane-N_2O gas (Abbott GmbH) and, after laparotomy, a 3 cm-long intestinal segment was exteriorized and exposed to a single dose of 19 Gy using an Elekta Synergy Platform delivering 4 MV X-rays at 2.3 $Gy.min^{-1}$. Sham-irradiation (sham-IR) was performed by maintaining the intestinal segment exteriorized without radiation exposure. After radiation exposure or sham-IR, the exposed segment was returned to the abdominal cavity and peritoneum/abdominal muscles and skin were separately closed with interrupted sutures.

Estimation of the number and volume of cells

For HUVEC counting and cell volume estimation experiments, cells were trypsinized (trypsin-EDTA, Life Technologies) and then counted by a TC20 Automated Cell Counter (Biorad) in the presence of trypan blue (Biorad) to estimate mortality. Cell volumes were calculated from the mean diameters determined by the TC20 Automated Cell Counter.

RNA extraction

For mRNA analysis, RNAs were prepared using the Rneasy Mini Kit (Qiagen). For miRNA analysis, total RNAs were prepared using the mirVana miRNA isolation kit (Thermo Fisher Scientific). RNA concentrations were quantified on a NanoDrop ND-1000 apparatus (NanoDrop Technologies), and miRNA quality was checked using an Agilent Bioanalyser. Experiments were performed in 3 replicates for each dose of irradiation and each time point of the kinetic.

mRNA expression analysis

Reverse transcription was performed using the High Capacity Reverse Transcription Kit (Thermo Fisher Scientific) according to the manufacturer's instructions. For targeted transcriptomics studies, gene expression assays were performed using pre-made TaqMan low-density 384-well arrays (TLDA) for human angiogenesis, inflammation, apoptosis, immune response and protein kinase panels (Thermo Fisher Scientific). cDNA (400 ng per sample) was loaded onto the port of each gene signature array card and PCR was performed using the ABI PRISM 7900 Sequence detection system (Thermo Fisher Scientific). Data Assist software (Thermo Fisher Scientific) was used to determine $2^{-\Delta\Delta Ct}$ values, with the following criteria: a maximum allowable Ct value at 37 was set and maximum Ct values were not included in calculations. Normalization was performed using a global normalization method on a per sample basis (Mestdagh et al., 2009). For specific gene expression studies, pre-developed TaqMan Gene Expression Assays (Thermo Fisher Scientific) were used and PCR was performed with the ABI PRISM 7900 Sequence detection system. For *in vitro* experiments, PCR fluorescent signals were normalized to a PCR fluorescent signal obtained from the housekeeping ACTB gene (for mRNAs) or the U6 snRNA (for miRNAs). For *in vivo* experiments, normalization was performed using the global normalization method on a per sample basis as indicated above. For unsupervised hierarchical clustering analyses and heatmap creation using Data Assist software, distances between samples were calculated for hierarchical clustering based on the ΔCT values using Pearson's correlation, assay centric as map type, and average linkage as clustering method.

miRNA expression analysis

Reverse transcription and qPCR were performed using different MegaPlex Human Pools (Thermo Fisher Scientific). RT MegaPlex and preamplification were performed on an Eppendorf Mastercycler Ep Gradient according to manufacturer instructions. We first evaluated microRNAs expression in HUVECs using RT Megaplex pool primers and TaqMan Array MicroRNA A and B Cards (759 microRNAs) (Thermo Fisher Scientific) using quantitative PCRs with the ABI PRISM 7900 Sequence detection system (Thermo Fisher Scientific). We selected a list of 312 microRNAS expressed in control and irradiated HUVECs 4 days post-irradiation by applying a cut-off with a maximum allowable CT value at. We next designed 4 custom TaqMan Array MicroRNA Cards to assess the expression level of the 312 microRNAs. In each card, a panel of 4 housekeeping microRNAs was included (Thermo Fisher Scientific). These 312 miRNAs were measured in triplicate at 0.5, 1, 2, 3, 4, 7, 14 and 21 days after 0 and 20 Gy. The global matrix was analyzed using Data Assist software (Thermo Fisher Scientific) and a final list of 289 miRNAs was used for implementation in the computational analysis including all biological entities.

Protein expression analysis

Protein extraction. HUVECs were washed 3 times with PBS and lysed, strongly vortexed and sonicated for 5 min in 1 mL of protein extraction buffer containing 8 M urea (Sigma), 100 mM triethylammonium bicarbonate buffer pH 8.5 (Thermo Fischer Scientific) and cOmplete Mini EDTA-free Protease Inhibitor Cocktail (Sigma-Aldrich). After addition of 0.03% (v/v) of ProteaseMAX Surfactant, Trypsin Enhancer (Promega), samples were incubated for 45 min at room temperature, centrifuged at 20,000 × *g* for 1 h and the supernatants were collected. Protein concentration was determined using the BCA protein assay kit (Sigma-Aldrich). Experiments were performed in 4 replicates for each time point of the kinetic and each dose of irradiation.

Peptide fractionation. Protein samples were reduced with 5 mM Tris-(2-carboxyethy) phosphine (Sigma-Aldrich) at 37°C for 1 h and alkylated with 60 mM iodoacetamide (Sigma-Aldrich) at room temperature in dark for 30 min. Then, 200 μg of protein were digested overnight at 37°C with 3.5% (W/W) sequencing grade modified porcine trypsin (Promega). 100 μg of the digests were dried in a SpeedVac concentrator (Thermo Fisher Scientific) and labeled with iTRAQ in a 4-Plex experimental design (114 and 116 reagents for control samples, 116 and 117 reagents for treated cells) as per the standard protocol supplied by the manufacturer (SCIEX). After labeling, samples were pooled and dried with the SpeedVac concentrator prior to peptide fractionation by isoelectric focusing. To perform peptide fractionation, 3100 OFFGEL Fractionator and the high resolution OFFGEL Kit (linear pH 3–10 gradient, 24 fractions) from Agilent Technologies were used as per the user's guide protocol. After focusing, each fraction was concentrated with a SpeedVac concentrator prior to LC-MS/MS analysis.

Liquid chromatography–electrospray ionization MS and data analysis of proteins. Peptides were re-suspended in 15–80 μL of 3% (v/v) acetonitrile/0.2% (v/v) formic acid depending on the initial volume of the fraction and then analyzed with a nano-LC1200 system coupled to a Q-TOF 6520 mass spectrometer equipped with a nanospray source and an HPLC-chip cube interface (Agilent Technologies). Briefly, peptides were enriched and desalted on a 160-nL RP-C18 trap column and separated on a Zorbax C18 column (30-nm pore size, 5-μm particle size, 150-mm long 75 μm inner diameter; Agilent Technologies) using a 55-min linear gradient (3–75% acetonitrile in 0.1% formic acid) at a flow rate of 400 nL/min. Full autoMS1 scans from 290 to 2,400 m/z and autoMS2 from 59 to 3,200 m/z were recorded. In each cycle, up to five precursors sorted by charge state (preferred 2 + ions and single-charge ions excluded) were isolated and fragmented in the collision cell. The collision cell energy was automatically adjusted according to the m/z ratio. Active exclusion of these precursors was enabled after 1 spectrum in 0.2 min, and the precursor selection threshold was set at 1,000 counts. Peptide and protein identification were performed using the Spectrum Mill MS Proteomic Workbench (Rev B.04.00.127; Agilent Technologies). The following parameters were used for data extraction: MH + mass range from 600 to 4,000, scan time range from 0 to 300 min, similarity merging of scan with same precursor (+/− 15 s and 0.05 *m/z*) and minimum MS s/n set to 25. The searches were performed with the following specific parameters: enzyme specificity, trypsin; two missed cleavage permitted; iTRAQ (N-term, K) fixed modifications; variable modifications, methionine oxidation, cysteine carbamidomethylation and Gln pyro-Glu (N-ter Q); maximum ambiguous precursor charge set to 3; mass tolerance for precursor ions, 20 ppm; mass tolerance for fragment ions, 50 ppm; ESI-QUAD-TOF as instrument; taxonomy, Human; database, SWISS-PROT release 20,170,315; 50% minimum scored peak intensity; calculate reversed database scores and dynamic peak thresholding. Identified proteins and peptides were auto-validated using default parameters. Validated peptides were then exported in an Excel.ssv file using the following filter parameters: score of peptides >6 and % of SPI >60. Last, differential protein expression of iTRAQ labeling data was performed using iQuantitator open source software and the eDesign default parameter value as described (Schwacke et al., 2009).

Metabolite expression analysis

Preparation of metabolites. HUVECs were washed with PBS, trypsinized, pelleted and stored at −80°C. Five million cells per experimental condition were vortexed for 2 min with cold (−80°C) 80% methanol for the precipitation of proteins. After 30 min at −80°C, the mixture was centrifuged for 10 min at 4°C, 14,000 × *g*. Supernatants were evaporated under a gentle stream of nitrogen and the dry extracts were resuspended in 70 μL of a 20% acetonitrile solution. Experiments were performed in 5 replicates for each time point of the kinetic and each dose of irradiation. 20 μL of each sample were gathered to obtain a pooled sample used as a quality control. A set of diluted pool samples was prepared making pools diluted 2, 4, 8, 16 and 32 times. The Mixture used for dissolution of dry extracts was also used as blank sample.

Ultra-high-performance liquid chromatography-high resolution mass spectrometry analysis of metabolites. Extracted metabolites were analyzed using reverse phase liquid chromatography hyphenated to high-resolution mass spectrometry. Chromatographic separation was carried out on a Dionex UltiMate 3,000 (Thermo Fisher Scientific) operated by Chromeleon 6.8 software. 5 μL of each sample was injected in a Hypersil Gold (100 mm × 2.1 mm x 1.9 μm) column (Thermo Fisher Scientific). The column was kept at 40°C and the flow rate was maintained at 400 μL/mL. Mobile phases were 0.1% formic acid solutions in water (A) and acetonitrile (B). For the first minute, a 0% of B was kept isocratically following by 10 min of linear gradient up to 100% B which was maintained in isocratic mode for 2 min. Initial conditions were reached in 1 min and the column equilibrated for 2 min. Along with chromatographic separation, mass spectrometry analysis was performed on the Q-Exactive Plus hybrid mass spectrometer (Thermo Fisher Scientific) with a Heated Electrospray Ionization (H-ESI II) probe working in the positive and negative ionization modes. Spray voltage was maintained to a ±3,500 V. Transfer capillary was heated to 320°C, sheath and auxiliary gas flow rates were maintained at 30 and 8 arbitrary units and the gas was heated to 310°C. S-lens RF was kept at 55 V in order to transfer ions of large *m/z* range toward the orbitrap mass analyzer. Mass spectra were acquired in the 80–1,000 *m/z* range. Each scan was acquired by collecting the ions into the C-trap during up to 250 ms in order to obtain spectra with 35,000 FWHM (Full Width Half Maximum) resolving power for the theoretical *m/z* 200. Instrument setup and LC-MS system control were achieved under Xcalibur 3.0.63 spectrometer software (Thermo Fisher Scientific) and control of the mass spectrometer was achieved using Tune Q Exactive Plus 2.5 application (Thermo Fisher Scientific). The samples were analyzed in the following order: blank samples were analyzed 5 times, then diluted pools were analyzed in triplicate from most diluted to least diluted, followed by experimental samples in random

order and spaced every 5 samples by a pool sample. At the end, a pool sample was subjected to a High Collision Dissociation (HCD) experiment using Data Dependent Analysis in order to obtain structural information from the MS/MS spectra.

Pre-processing of metabolomics data. Raw data were converted into mzXML files using ProteoWizard (Chambers et al., 2012). Data extraction was achieved using XCMS library under the R environment for the positive and negative ion modes separately. Peak detection was performed using the centWave method. Chromatographic peak width was set from 2 to 15 s, signal to noise threshold at 3, while the noise was set to 10,000 and the *m/z* tolerance between two consecutive scans was set to 5 ppm. Pre-filtering of detected peaks was set to 4 consecutive scans with intensities higher than 50,000. Peak alignment between samples and peak grouping were achieved using the Obiwarp algorithm and density method, respectively. Extracted data matrices were then filtered in order to eliminate analytical background and correct analytical drift. Peaks coming from the blank samples and from instrument noise were removed from the matrix, together with any peaks that varied by more than 30% in all pool samples. Peaks in diluted samples that did not linearly increase in line with concentration were removed for all samples. Analytical batch drift was corrected using the van der Kloet algorithm (van der Kloet et al., 2009). The final matrices contained 661 ions in the positive ionization mode and 658 ions in the negative mode. The two-ionization matrices were used separately for the untargeted metabolomics analysis. For the semi-targeted approach, matrices were matched to our in-house database, containing retention time and *m/z* information on about 1,300 metabolites for the peak annotation. Matching was performed using Workflow4Metabolomics (Giacomoni et al., 2015), using the LC-MS annotation with bank in-house tab (Rochat, 2017). The final matrix contains 115 metabolites identified with different levels of identification. Prior to statistical analysis, metabolite intensity is normalized by row, i.e. dividing it by the addition of metabolite intensities in all the samples. Next, we "autoscale" the matrix by mean-centering each metabolite and then multiplying by the inverse of its standard deviation.

Omics data visualization and denoising

Before any analysis, the data were projected into a three-dimensional space using the *t*-distributed stochastic neighbor embedding (t-SNE) method (van der Maaten and Hinton, 2008). The aim of such translation was to explore the eventual presence of recurrent profiles, both in time and in expression.

Since only the protein dataset was expressed in fold-change terms, and with a view to completing a homogeneous comparison, we linearly regressed to their fold-change-like ratio transcripts, metabolites and miRNAs. This may be calculated by solving the following optimization problem (Morilla and Ranea, 2017):

$$y = X\beta + \delta,$$

where typically y is the vector of observed values, i.e. up- or downregulated relative to their prior measurement, $X\beta$ the product between the matrices X (dataset expression) and β (variable to be calculated), and δ is the correlated random error which follows a normal distribution.

Additionally, those molecular entities with an associated confidence interval of Z-scores ranging [-1, 1] in multi-testing were considered as unchanged and consequently removed from the initial analysis of the omics models. These discarded entities were only recovered if they were functionally enriched in some GO (Ashburner et al., 2000) or Panther (Mi et al., 2019) terms in the following functional analysis step.

Construction of the irradiated complexes

In this step of the analysis, we intended to contract the discrete space determined by the projection of the data denoised in the previous section to a continuous space. The rationale underlying this transformation was to identify lasting modules. To this end, we constructed simplicial complexes making use of the Vietoris-Rips filter (Hausmann, 1995), which provides a suitable method for associating vector spaces using linear maps. This topological configuration (i.e. the nerve theorem (Borsuk, 1948)) would enhance by homology (Stillwell, 1993) those clusters relevant to successfully completing the entire conversion. Those clusters are referred to as persistence modules and within them, they contain precious information on the high dimensional structure of any natural dataset.

Filtered simplicial complexes of proteins, transcripts, metabolites and miRNAs were carried out by means of in-house scripts using Javaplex software (Adams et al., 2014), the R package Mapmate (Leonawicz, 2017)

and the FFmpeg (Korbel, 2012) function in R. The homological assembly was performed in two steps. First, the Vietoris-Rips filter coordinates and simplicial alpha complex chains were calculated using Javaplex. both coordinates and chains information were then used as input in a Mapmate-based R script. This script captures the trace of each homology variance resulting during the conversion in individual frames. Last, we take the FFmpeg function to neatly glue each of these frames in a video tracking the whole conversion between spaces.

Summary of the topological invariants in the datasets: barcodes landscapes and silhouettes

Next, we summarized the structural information encapsulated in the persistence modules considering barcodes (Carlsson et al., 2005) at different dimensions, a notion based on the durability that two topological subspaces are approached as homologically independent within the same complex during the construction of the filtered simplicial complex. Given an interval *IinR* and a persistence module $M = M_t$ we defined the indecomposable persistence modules as interval modules $(I_m)_t$ equal to the filtration complex if $t\epsilon I$ or 0 otherwise. Hence M is a direct sum of these interval modules [Gabriel, Zomorodian-Carlsson, Crawley-Boevey Theorem (Oudot, 2015)]. Last, we denominated barcodes to the random variable composed by the set of possible intervals $[I_k]$ (Bubenik, 2015) agreeing with that theorem. other versions of the barcodes, such as landscapes (i.e. a continuous and stable barcode) (Bubenik, 2015) or silhouettes (smooth piecewise barcodes) (Chazal et al., 2015) were also explored during this step in the analysis.

The barcodes along with their related other versions summarizing the filtered simplicial complex were computed on each dataset by tailored R scripts based on TDA package, version 1.6.9 (Fasy et al., 2019).

Mapping of topological invariants

Another in-house script, based on the Mapper algorithm (Singh et al., 2007) and its python module Kepler mapper (Kmapper) (van Veen and Saul, 2019), was developed to perform the mapping between the persistence modules identified by their barcodes, landscapes or silhouettes and their projections in R^2. This mapping gave us the simplicial complex in a graphical form which is very practical for our purposes: the mapper graph.

First, we automatically detected samples that are different from regular samples by means of anomaly detection algorithm (i.e. isolation random forest) generating a 1-D lens or filter function that is a lower dimensional representation of data (van Veen and Saul, 2019). Then, we built another 1-D lens with t-SNE projection and combine both lenses to create a 2-D lens. Next, we created the simplicial complex as indicated in the preceding sections. The existence of some cyclic temporary periods found in our datasets penalizes the use of the Hausdorff distance as the default measure applied in the filter. Instead, we used the more convenient Dynamic Time Warping (DTW) distance (Lauwers and De Moor, 2017):

$$d_{DTW}(y_1, y_2) = min\left\{\sqrt{\sum_{k=1}^{K} w_k}\right\},$$

where $w_k = (y_1(l) - y_2(m))^2$ with the $(l,m)-th$ element of the matrix determined by the time series y_i. Since the time points were discriminated later at D14 and D21, the alignment of the curves was done earlier, between 12 h and D7. Then, the sum over the path W_{DTW} is the DTW distance. Hence, we constructed the map induced by the nerve of the simplicial complex cover composed of 15 clusters, the so-called *cubes*, which may overlap by up to 50%, and used the K-means method (Lloyd, 1982) to group the cubes with the DTW distance. Last, an interactive html file was created to clearly visualize the graph.

Functional analysis of persistent candidates

At this stage, the mapping produced ad described in the previous section was functionally examined under the prism of GO annotations. We searched for enriched terms in the set of persistent candidates that might reveal relevant biological pathways and processes involved in the response to irradiation. In addition, we implemented a Python API to query the Panther database. Moreover, the Pathway Studio Web Mammal software, version 12.4, querying the Mammal (Anatomy; CellEffect; DiseaseFx; GeneticVariant; Viruses) version 12.4.0.3 (Updated April 25, 2021) database from Elsevier (www.elsevier.com/pathway-studio) (Nikitin et al., 2003) and the g:Profiler webtool (Raudvere et al., 2019) were also used in the functional analysis of the candidates.

Integrated omics-graph construction

The molecular identities we identified do not work independently. There is an intricate exchange of information at many levels that determines their global function in the endothelial cells. To untangle such a complex of wired regulatory interactions, we constructed an overall gene regulatory network (OGRN). The GeneMANIA webtool (Warde-Farley et al., 2010) worked as primary reference (Lees et al., 2015) to construct this OGRN. Thus, the persistent candidates obtained in the earlier sections were the bricks used to build the OGRN. In particular, we considered DIANA Tools (Vlachos et al., 2012) to detect the most likely experimental or predicted miRNA-target interaction. For the metabolite dataset, we used the metabolite-protein interactome publicly available in the Human Metabolome Database (HMDB) (Wishart et al., 2018). If no information could be retrieved from HMDB for a specific metabolite, we retrieved related terms instead.

Graph convolutional networks of integrated omics-graph

A deep learning model on the OGRN composed of the persistent candidates was presented in the last step of the analysis. This model somehow accurately predicts how differentiated molecular entities involved in relevant processes of radiation-induced dysfunction evolve in terms of feature representation, i.e. early or late irradiation response. To build the model, we equipped the OGRN with a convolutional design (i.e. neural networks) and a spectral rule of node aggregation similar to graph convolutional networks (GCNs) (Defferrard et al., 2016) in order to extract and exploit the complex information contained in its dynamic graphic structure. Two hybrid sequential models were combined to learn the endothelial cells progression after irradiation: (1) using the identity matrix I as features and the adjacency matrix A to build the model using the spectral rule:

$$sr(A, I)_i = \sum_{j=1}^{N} \frac{1}{D_{i,i}^{0.5}} A_{i,j} \frac{1}{D_{j,j}^{0.5}} I_j$$

where D the degree matrix, and (2) considering the distance of the shortest path to acute and late cell dysfunction as an additional feature. These models were designed in two layers with 512 units in the layers and a 2D transformation of the activation function *tanh*. Instead, the *relu* activation function was applied in the spectral rule at the beginning of the layer implementation. The number of epochs was set to 5,000 and 250, respectively. We applied the stochastic gradient descent (sgd) optimizer during the training with a learning rate and momentum regularization set to 0.001 and flagged true, respectively.

An in-house python script based on MXNet implementation (Cruchant, 2020) performed the semi-supervised classification (early or late response) of nodes in the OGRN graph (Kipf and Welling, 2016).

siRNA and miRNA mimic transfection

HUVECs were transfected at 50–60% confluence with 100 nM of non-targeting siRNA or siRNA targeting SERPINE1, CD44 or CDKN2A (Thermo Scientific), or with 50 nM of miR181a or miR181c mimics (Thermo Scientific) using Dharmafect (Thermo Scientific) as transfection reagent. Cells were lysed for RNA extraction as described above at the times indicated post-transfection. Knockdown efficiency was measured by RT-qPCR.

In vitro tube formation assay

HUVECs were trypsinized 48 h after transfection. BD Matrigel Basement Membrane Matrix (BD Biosciences) was added to 24-well plates and allowed to solidify at 37°C. Once the Matrigel solidified, HUVECs were re-seeded into Matrigel-coated wells (180,000 per well) and irradiated as described earlier. Angiogenic ability was assessed 18 h after re-seeding and irradiation by evaluating the total number of junctions after observation under a light microscope and the use of the Angiogenesis Analyzer plugin of ImageJ version 1.52a software (National Institutes of Health).

β-gal staining

At the indicated time following 0, 2 or 20 Gy, cells were stained using a β-Gal Staining Kit (Thermo Fischer Scientific) according to the supplier's instructions.

QUANTIFICATION AND STATISTICAL ANALYSIS

For the proteomics dataset, we used iQuantitator software which is based on a modeling approach, statistical methods and tools for estimating relative changes in protein expression under different treatments and experimental conditions (Schwacke et al., 2009). Parameter inference in iQuantitator uses computational methods developed using the Bayesian statistical framework. As a result, the normalized expression data are means $\pm$ credible intervals. A differential expression is statistically significant (noted with * on the graphs) when the 95% credible interval does not contain 1 (the null effect). For other datasets, results are expressed as mean $\pm$ SEM. When the data meet the normality assumption (Shapiro-Wilk), we performed t-tests and one-way ANOVA followed by multiple comparisons tests (Tukey, Dunnett or Sidak). Otherwise, we used non-parametric statistical tests (Mann-Whitney Rank-Sum Test or Kruskal-Wallis one-way ANOVA on Ranks). All p values were corrected for multiple comparisons tests (Tukey or Dunn's). The type of test used is indicated in the figure legend for each dataset. A p value of <0.05 was considered statistically significant. *, $p < 0.05$; **, $p < 0.01$; ***, $p < 0.001$; ****, $p < 0.0001$ for indicated comparisons, error bars represent standard error of means. The tests were performed using GraphPad Prism, version 8.1.1 for Windows, which was also used to build the graphs.